2021

# CONCENTRATION AND COMPOSITION OF NANOPARTICLES AND COLLOIDAL PARTICLES IN A MINE-WASTE CONTAMINATED RIVER

Kaitlin Rose Perkins
*University of Montana, Missoula*

# CONCENTRATION AND COMPOSITION OF NANOPARTICLES AND COLLOIDAL PARTICLES IN A MINE-WASTE CONTAMINATED RIVER

By

KAITLIN ROSE PERKINS

Bachelor of Science, Washington State University Vancouver, Washington, 2017

Associate of Science, Clark College, Vancouver, Washington, 2013

Thesis
presented in partial fulfillment of the requirements
for the degree of

Master of Science
Systems Ecology

The University of Montana
Missoula, MT

April 2021

Approved by:

Scott Whittenburg, Dean of The Graduate School
Graduate School

Benjamin P. Colman, Chair
Department of Ecosystem and Conservation Sciences

Alysia Cox
Chemistry & Geochemistry Department
Montana Technological University

Bob Hall
Division of Biological Sciences

Nancy Hinman
Geosciences in College of Humanities and Sciences

Perkins, Kaitlin, M.S., Spring 2021 Systems Ecology

Concentration and composition of nanoparticles and colloidal particles in a mine-waste contaminated river

Benjamin P. Colman

Metals and metalloids (metal(loid)s) in aquatic ecosystems are often described through measures of their concentrations in whole and filtered waters. The filtered fraction is operationally defined as “dissolved,” and assumed to be primarily composed of free metal(loid) ions or of ions bound by low molecular weight organic matter. This definition ignores that the dissolved fraction also likely contains colloidal particles (1 to 1000 nm) that can pass through commonly used filters. This colloidal fraction can also be preferentially removed from the water column by algae and other aquatic organisms compared to free metal(loid) ions and organic bound metal(loid)s. Though they may be important in describing the bioavailability and toxicity of contaminants, the abundance and composition of colloidal particles is not well described. To better understand the abundance and elemental composition of colloidal particles in aquatic ecosystems, we used single particle inductively coupled plasma time-of-flight mass spectrometry (spICP-TOFMS) to simultaneously characterize and quantify a range of elements in individual colloidal particles. We collected samples from eight mainstem sites and two tributaries to the Clark Fork River, Montana, which has a legacy of metal(loid) contamination in its sediments and surface waters from past mining and ore processing. Colloidal particles were abundant in all samples, with 144 different particle types detected. The most common particle types contained Fe and Mn. Single-element particles were more abundant than multi-element particles, however our estimate of multi-element particles is likely conservative due to the small size of the single-element particles (median 83 nm) which may limit detection for minor components. Multi-element colloidal particles mostly consisted of Fe and Mn in combination with other metal(loid)s, indicating Fe and Mn may serve as vectors for more toxic metal(loid)s. Our data suggest biogeochemistry drove the presence of the abundant Fe and Mn containing particles, which contrast with the Al and Si rich sediment. The small size of the colloidal metal(loid) particles suggests that that contaminant exposure to organisms occurs as complex assemblages of colloidal particles. Loads of elements in colloidal particles increased for many elements from upstream to downstream, though the exact mechanisms behind this increase are unknown. The abundance of colloidal particles in this study suggests that they may be important to the fate and transport of metal(loid) contaminants, and that they may be important to consider when examining exposure, accumulation, and toxicity of metal(loid) contaminants in aquatic ecosystems.

## Contents


1. Introduction ..... 1
2. Methods ..... 5
   2.1 Site history ..... 5
   2.2 Site description ..... 6
   2.3 Sample collection ..... 7
   2.4 spICP-TOFMS ..... 8
   2.5 Data processing ..... 9
   2.6 Common and rare particles ..... 10
3. Results ..... 11
   3.1 Study reach discharge and water chemistry ..... 11
   3.2 Particle Characteristics ..... 12
      3.2.1 Particle composition ..... 12
      3.2.2 Size of metal oxide particles ..... 16
   3.3 Spatial Patterns ..... 18
      3.3.1 Longitudinal abundance, concentration, and load of particle types ..... 18
      3.3.2 Longitudinal concentration and load of elements ..... 22
4. Discussion ..... 25
   4.1 Nanoparticles and larger colloidal particles may be contaminant vectors ..... 26
   4.2 Biogeochemistry was a driver of colloidal particle composition ..... 27
5. Summary ..... 29
6. References ..... 30
Appendix A. Data processing ..... 35
   A.1 Calibration ..... 35
   A.2 Element mass ..... 35
   A.3 Discharge interpolation ..... 35
   A.4 Common particles ..... 35
   A.5 Number of moles per particle by element ..... 36
   A.6 Oxide particle size ..... 36
   A.7 Mass concentration and load ..... 36
   A.8 Particle concentration and load ..... 36
Appendix B. Generalized Additive Modeling ..... 36
Appendix C. Tables ..... 37

Table 2. Site coordinates and corresponding USGS gages ..... 37
Table 3. Environmental data in order from most upstream (WS) to most downstream (CF8) ..... 38
Table 4. Median number of attomoles per particle ..... 38
Table 5. Particle size summary statistics ..... 40
Table 6. Particle size summary statistics by number of elements per particle ..... 41
Table 7. Relative number of particles ..... 41
Table 8. Generalized additive model fitted values for particle concentration and load. ..... 43
Table 9. Generalized additive model p-values and r-squared values for particle numerical concentration and load. ..... 45
*These values are based on the significance of the smooth terms of the model. ..... 45
Table 10. Generalized additive model fitted values and standard error for element concentration and load. ..... 46
Table 11. Generalized additive model p-values and r-squared values for element concentration and load. ..... 49
Table 12. Limit of detection values for each element ..... 49
Table 12: Comparison of mass concentrations for Fe vs. Al and Si ..... 50
Table 13: Comparison of number of particles with Fe vs. Al and Si ..... 50
Table 14: Load change following mixing of Little Blackfoot and the Clark Fork. ..... 51

# 1. Introduction

Studies examining the concentrations and cycling of metals and metalloids in aquatic ecosystems often focus on either unfiltered or filtered water samples. The concentration of metals and metalloids (hereafter metal(loid)s) in the filtered sample is defined as being "dissolved," and metal(loid)s in the dissolved fraction are assumed to consist largely of either free ions, metal(loid)s bound by dissolved organic matter, or other ionic species of metal(loid)s like soluble oxides and hydroxides (Aiken, Hsu-Kim, and Ryan 2011). While the bioavailability of species in the dissolved fraction differ relative to one other, the dissolved fraction is often the focus in studies examining the exposure, accumulation, and toxicity of metal(loid)s to aquatic organisms (de Paiva Magalhães et al. 2015).

One weakness of this definition of the dissolved fraction is that it ignores the fact that commonly used filter sizes (0.2, 0.45, or 0.7 µm) allow colloidal particles (1 to 1000 nm) to pass through, and some metal(loid)s occur in surface waters in the colloidal size fraction (Guéguen and Dominik 2003; Farag et al. 2007; Stolpe et al. 2013). Colloidal particles containing Fe and Mn are abundant in rivers and streams and can act as vectors for other metal(loid)s (Hassellöv and von der Kammer 2008). Colloidal Fe particles form from the oxidation of dissolved $Fe^{2+}$ in both surface water and riverbed sediments (Fox 1988; Ratié et al. 2019). Other metal(loid)s also occur in the colloidal pool in rivers and streams alongside Fe and Mn, including Al, Cu, Pb, and As (Farag et al. 2007; Trostle et al. 2016).

Though metal(loid)s in the colloidal size fraction might be less available than if they were in ionic form, colloidal particles can be more biogeochemically active when compared to truly dissolved metal(loid)s. For example, in mesocosms containing floating treatment wetlands,

metal(loid)s that were abundant in colloidal particles were removed from the water column to a greater extent than "truly dissolved solutes" (filtrate < 1 nm), and this process was facilitated by the periphyton (the assemblage of algae, bacteria, and fungi) growing on plant roots in the water column (Sullivan 2019). In a review of engineered nanoparticles (1 – 100 nm), the authors described the importance of these particles in the sequestration and transformation of inorganic nanoparticles (Desmau et al. 2020).. Silver nanoparticles cause stress to aquatic macrophytes (Yuan et al. 2018). In experimental streams exposed to Cu and Zn with Fe oxide particles, the periphyton had both enhanced metal accumulation and reduced growth rates compared to a treatment without Fe particles (Cadmus et al. 2018). Multi-element particles containing hydrous Fe oxides with Cu sorbed to the surface were found to be a source of dietary exposure to Cu for benthic grazing aquatic macroinvertebrates (Cain, Croteau, and Fuller 2013). Freshwater snails accumulate zinc oxide particles that were internalized by diatoms through a dietary exposure pathway (Croteau et al. 2011). While the cycling and bioavailability of colloidal particles has been well-documented in laboratory studies, there is still much to be understood in field studies of rivers and streams.

To understand the nature of colloidal particles in ecosystems, methods are available that can describe colloidal particle at the level of their bulk characteristics or at an individual particle level. Methods in bulk characterization often employ a two-step process including size-separation of the sample followed by characterizing the concentration or speciation of elements. One approach is to separate colloidal particles based on size using sequentially smaller filter sizes in the micrometer to nanometer size range, followed by ICP-MS analysis (Sigg et al. 2000; Guéguen and Dominik 2003; Farag et al. 2007; Colman et al. 2014; Trostle et al. 2016). This "cascade filtration" approach does not distinguish between metal(loid)s in a given size fraction

that are bound to colloidal organic matter as opposed to metal(loid)s found as colloidal mineral particles; however, subsequent analysis of the retained particles using X-ray diffraction can give insights into dominant crystalline phases while X-ray absorbance spectroscopy can provide insights into major and minor chemical species (Bone et al. 2012). As an alternative to using discrete size-based cutoffs for separating colloidal particles, techniques such as field flow fractionation can separate particles based on either hydrodynamic radius or buoyant volume before characterization of the separated particles. Colloidal particles can be characterized with a variety of inline detectors including light scattering detectors which can measure particle size and fractal geometry, as well as destructive analysis through ICP-MS (Kammer et al. 2011). These bulk techniques provide rich data about the composition of the entire assemblage of particles within a given particle size or size fraction, but they do not provide the chemical composition of individual particles.

For characterizing individual-particles, commonly used methods include electron microscopy and single particle inductively coupled plasma mass spectrometry (spICP-MS). Electron microscopy can leverage a range of techniques that can both image the surface and interior of colloidal particles, and provide detailed information about particle shape, size, and crystal structure. When paired with energy dispersive spectroscopy or electron energy loss spectroscopy, electron microscopy can also provide information on composition. Electron microscopy can also be used with size-separated fractions generated through cascade filtration or field flow fractionation (Plathe et al. 2010). The main challenges with electron microscopy are that throughput is limited when analyzing individual particles, and composition information is semi-quantitative (Scimeca et al. 2018). The use of spICP-MS provides complementary insights into particle composition. With the use of shorter, µs dwell times in a quadrupole MS, spICP-MS can

capture up to two elements in particles simultaneously and with increased sample throughput (Montaño et al. 2019). Though spICP-MS excels at characterizing the mass of one element in a large number of individual colloidal particles, and while it can be used to examine two elements simultaneously in newer instruments, it cannot characterize particles with a larger number of elements, such as those that might be expected in surface waters (Montaño et al. 2019).

Though early work using spICP-MS was focused on detecting manufactured nanomaterials in surface waters, new advancements show promise for greatly expanding our ability to characterize natural and incidentally formed colloidal particles (Montaño et al. 2019). The coupling of spICP-MS with a time-of-flight (TOFMS) mass analyzer has led to techniques in single particle inductively coupled plasma time-of-flight mass spectrometry (spICP-TOFMS). With spICP-TOFMS, we can rapidly characterize many elements simultaneously in individual particles, allowing us to rapidly screen thousands of particles in rivers and streams.

Despite the known presence of colloidal particles in surface waters, colloidal particle abundance and characteristics like their composition and particle size in natural systems are not well described. The goal of this study was to characterize metal(loid) particles in the mine-waste contaminated Upper Clark Fork River in Montana during base flow, and to do so on a quantitative particle-by-particle basis. Increasing our understanding of the composition, abundance, size, and load of colloidal particles moving through this contaminated river is the first step in understanding the forms of metal(loid)s that organisms are exposed to and may provide insights into the patterns and potential mechanisms contributing particles to the water column during baseflow.

# 2. Methods

## 2.1 Site history

Hard rock mining took off in the Upper Clark Fork River (UCFR) basin in the late 1800s, after which Butte became a source for much of the copper that electrified the country in the early twentieth century (Brooks 2015; Helgen and Davis 2000). At one point during this period, the mines at Butte were some of the most productive copper mines in the world, however the processes of mining, ore processing, and smelting produced millions of tons of metal(loid)-contaminated waste that were deposited into the waterways and floodplains in Butte and Anaconda. In 1908, a flood redistributed these contaminants within the Upper Clark Fork watershed to floodplains, sediments, and water downstream (Nimick and Moore 1991; Brooks 2015). The contamination from these events was detected over 400-km downstream from the headwaters, with the highest contamination levels in the first 45-km of the river (Hornberger et al. 2009). The widespread contamination in UCFR floodplains and sediments led to it being established as the Clark Fork River Operable Unit (US Environmental Protection Agency 2004), which is part of the Clark Fork Superfund Complex (Figure 1)..

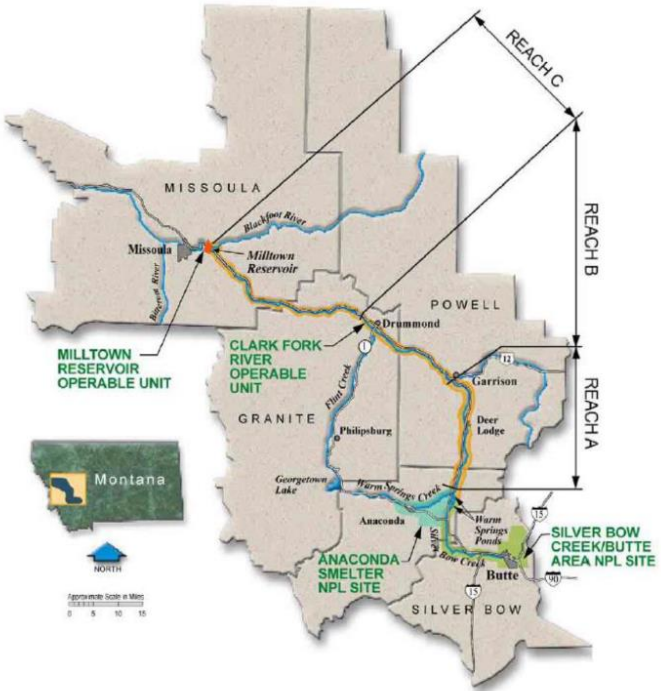

Figure 1: Clark Fork Superfund Complex (US EPA, 2004)

## 2.2 Site description

Our study focused on the first 69 km of the Clark Fork River Operable Unit, which has elevated levels of contamination, ongoing remediation and restoration, and ecological impairment. Designated by the US Environmental Protection Agency (US EPA) as "Reach A", it runs from the headwaters of the Clark Fork River at the confluence of Warm Springs Creek and Silverbow Creek to the Little Blackfoot River (US Environmental Protection Agency 2004). Reach A has been the site of extensive and on-going floodplain remediation and restoration efforts to meet remediation standards set by the US EPA and expanded by the Montana Department of Environmental Quality (MT DEQ). Work has included the removal of contaminated floodplain material before widespread bank stabilization and revegetation (Moore and Langner 2012). Despite the extensive remediation, aquatic invertebrates show evidence of continued impairment and trout populations remain low in the UCFR (Naughton et al. 2020; Cook et al. 2017). Reduced trout populations may be partially attributed to low water levels and elevated water temperature in the river during summer months, though these issues are likely exacerbated by persistent metal contamination (Cook et al. 2017).

The UCFR has been regularly monitored by the US EPA and MT DEQ for a range of contaminants and environmental characteristics. Metal(loid) contaminants of concern are monitored in surface waters and sediments and include metalloid arsenic (As) and the four metals cadmium (Cd), copper (Cu), lead (Pb), and zinc (Zn). In the 2018 monitoring report from the MT DEQ, the metal(loid) concentration targets were exceeded for all five metal(loid)s at some surface water stations, with As (61% of samples) and Pb (31% of samples) exceeding concentration goals more than Cu, Zn, and Cd. Sediment samples also exceeded established concentration goals and to a much greater extent; all sediment samples exceeded the probable

effect concentration (PEC) for As, Zn, and Cu and 75% exceeded the PEC for Pb and Cd (Naughton et al. 2019). The metal(loid) contaminants in the sediment may be acting as a chronic source of metal(loid)s to surface waters of the UCFR (Moore and Langner 2012).

### 2.3 Sample collection

We collected samples during baseflow over Reach A of the UCFR on September 28, 2018 (Table 1) from ten sites streamside along the river in what is the most contaminated reach. These sampling sites included eight mainstem UCFR sites and two of its tributaries. Several minor tributaries flowed into the river between sites but were not sampled. Spring and summer flows were high in the UCFR in 2018 and may have resulted in higher than normal metal(loid) concentrations (Naughton et al. 2019), while precipitation in the months prior to sampling was low and between 4% and 49% of the normal monthly values (NOAA 2018). We collected environmental data (dissolved oxygen, temperature, specific conductivity, and pH) concurrently with sample collection using a multi-parameter probe (YSI). Unfiltered water samples were collected in new 50-mL VWR polypropylene centrifuge tubes. The tubes were filled with ultrapure water days prior to collection, and the water was dumped on site just prior to sampling. Samples were immediately shipped to the University of Vienna. Dr. Manuel Montaño analyzed the samples using spICP-TOFMS to generate the data that we then used to characterize and quantify the mass, size, and composition of individual colloidal particles.

Table 1. Site abbreviation, name, and location for eight UCFR sites and two tributaries of the UCFR.

| Site | Site Name | Latitude | Longitude | Main/Tributary |
|---|---|---|---|---|
| WS | Warm Springs Cr | 46.18592 | -112.7738 | tributary |
| CF1 | Warm Springs | 46.18721 | -112.7703 | UCFR |
| CF2 | Perkins Rd | 46.20860 | -112.7676 | UCFR |
| CF3 | Galen Rd | 46.23743 | -112.7532 | UCFR |
| CF4 | Racetrack | 46.26538 | -112.7447 | UCFR |
| CF5 | Sager | 46.31738 | -112.7362 | UCFR |
| CF6 | Deer Lodge | 46.38350 | -112.7380 | UCFR |
| CF7 | Kohrs Bend | 46.49802 | -112.7412 | UCFR |
| LB | Little Blackfoot River | 46.51942 | -112.7934 | tributary |
| CF8 | Downstream of LBR | 46.51987 | -112.8077 | UCFR |

## 2.4 spICP-TOFMS

To investigate the elemental composition of individual colloidal particles, we analyzed samples with spICP-TOFMS (TOFWERK AG, Thun, Switzerland). Like spICP-MS using a quadrupole instrument, this method is a powerful tool for trace element analysis of inorganic colloidal particles. The use of a time-of-flight mass analyzer is that it allows us to obtain information about a wide range of elements in each individual particle as opposed to only one or two on an instrument with a quadrupole mass analyzer. As such, spICP-TOFMS has the potential to better address the need for elemental analysis in the complex matrix of natural waters (Montaño et al. 2019).

The instrument was calibrated with both nanoparticle and dissolved standards, and samples were diluted to minimize coincidence of particles and the instrument. The spICP-TOFMS system measures particles as peaks and dissolved material and noise as a background signal when measuring the ions that pass through the instrument. Using a 3 ms dwell time, particle peaks were separated from the background signal by calculating the mean signal intensity and standard

deviation, then identifying data as peaks when they were greater than three times the standard deviation of the mean of the background signal. The spICP-TOFMS instrument was calibrated using gold particle standards in two different formats: 60 nanometer particles at a concentration of 50 parts per trillion and 100 nanometer particles at 500 parts per trillion (BBI Solutions, Crumlin, UK). To calibrate the particle mass measurements, the results from measuring the calibration standards were modeled with other measured variables, including the instrument's transport efficiency, dwell time, and sample flow rate. The transport efficiency of spICP-TOFMS quantifies the incomplete transfer of particles from the gold nanoparticle standards to the instrument relative to dissolved ions and was calculated for this analysis using the 60 nm and 100 nm standards. Particle peaks were then converted to mass values for each element within a particle using calibration curves (see Appendix A for calibration curve equations and figures). We diluted samples one in one thousand to ensure a low concentration of particles. We analyzed a full spectrum of metal(loid)s within nano- and colloidal particles, including those monitored by the US EPA and MT DEQ.

### 2.5 Data processing

To process the expansive spICP-TOFMS output for this analysis, we coded a workflow in R Statistical Software (R 2020). For each element, we created a presence/absence matrix for each particle to delineate all the different particle compositions and allow for determination of particle counts by particle type. Particle sizes were calculated assuming that Fe, Mn, aluminum (Al), and silica (Si) were present as hematite, manganese dioxide, aluminum oxide, and silicon dioxide, respectively. Additionally, we assumed particles had a general bulk density of 2.65 g $cm^{-3}$ when calculating size based on the common mass assumption for soils and sediments (NRCS 2012). The number of moles per particle was calculated by converting mass values into moles within a

particle using the molar mass of each element. The confidence interval around the median of moles for each particle was estimating using the binomial distribution. Particles were quantified across all ten sites by both the number of particles present and the mass of metal(loid)s within particles. The concentration and instantaneous load of both the number of particles and metal(loid) mass were calculated by scaling up the volume of sample analyzed to a per liter measurement using the sample flow rate through the instrument and accounting for dilution. Loads were calculated using discharge values either collected from United States Geological Service (USGS) gages or interpolated from those data for sampling sites that are unavailable by using weighted means with linear regression modeling.

We used generalized additive models (GAMs) to explore how sites differed from each other in concentration and load along the river. Using GAMs to explore ecological data allowed us to capture non-linear patterns and penalizes the curviness of the model to prevent overfitting. All work was done within the R statistical environment (v. 4.1.0, R Core Team, 2021), and the GAMs for particle and element concentration and load were created using *mgcv* with the *REML* option for automated estimation of the smoothness parameter (Wood 2021). In this modeling approach, we applied a smoothing function to the predictor variable and estimated the smoothness parameters and selected a model using restricted maximum likelihood. The models were built with a single predictor variable, distance downstream from CF1, with the two tributary sites excluded from the model but presented on the figures.

### 2.6 Common and rare particles

In exploring our data, there were some particle types with >10,000 measured particles and others with only one detected particle. For many of our in-depth looks at individual particle types, we chose to focus on the most abundant particles, which we will refer to as “common” particles. We

defined common particles as being the top 20% of all particle types based on a rank abundance curve using approaches in microbial community ecology (Wilhelm et al. 2014). With the 20% threshold defining our common particles, we included particle types with at least 10 detected particles across all samples. The other 80% of particle types were categorized as “rare”. Rare particles were included in broader analyses of masses of elements in colloidal particles and numbers of single and multi-element particles but were excluded for the particle-specific characterizations for clarity.

# 3. Results

## 3.1 Study reach discharge and water chemistry

Moving from upstream to downstream in the UCFR, the river showed small increases in temperature, dissolved oxygen, and pH, and larger increases in discharge and specific conductance. The pH values increased from 8.5 to 8.9 over the sampling sites (Figure 2B). Dissolved oxygen was relatively constant between 10.6 to 11.6 mg $L^{-1}$ (data not shown) showing a slight trend towards increasing concentrations downstream. Water temperature increased slightly (7.2 to 8.6 °C) as they were sampled over the course of the morning from upstream to downstream, with the tributaries WS and LB having similar temperatures to their adjacent mainstem sites (Figure 2C). Specific conductance increased by 60%, increasing from 297 to 477 µs $cm^{-1}$ at WS and CF7, respectively (Figure 2D). Tributary LB had the lowest specific conductance, which was similar to WS. Discharge increased four-fold over the eight CF sites, increasing from 2.3 to 8.1 $m^3 s^{-1}$ (Figure 2E). The tributaries WS and LB had similar discharges (2.0 and 2.3 $m^3 s^{-1}$), and LB was approximately 1/3 that of discharge at CF7.

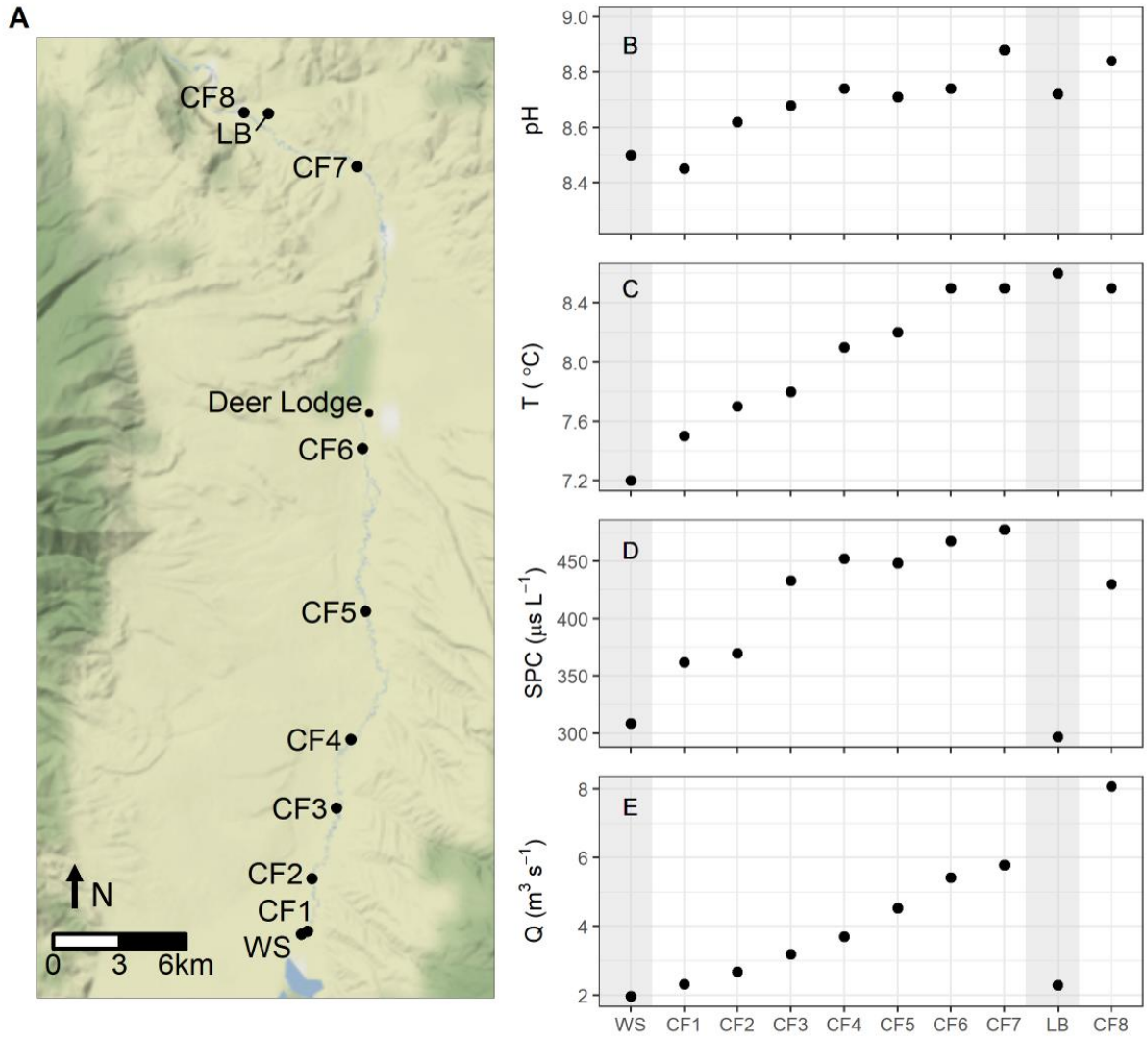


Figure 2: Site information including (A) site map where CF designates main stem and WS and LB are tributaries, (B) pH, (C) temperature (T, °C), (D) specific conductance (SPC, µS $L^{-1}$), and (E) discharge (Q, $m^3 s^{-1}$). Gray bars represent tributaries, and tributaries are positioned on the figure relative to where they enter the UCFR between other sample sites.

## 3.2 Particle Characteristics

### 3.2.1 Particle composition

*A profile of all detected particles*

For the eighteen elements we included in our analysis, we detected over 23,000 particles across our ten sites, with each particle containing between one and five detected elements. These

particles consisted of a total of 144 different particle types, where each particle type was named based on the elements of which it was composed. Most particles (81%) consisted of only one detected element, and generally, as the number of elements detected in particles increased, the number of those particles decreased. Of the 23,710 particles detected, 19,096 were single-element, 4,298 were two-element, 250 were three-element, 42 were four-element, and only 10 particles had five elements.

A deeper examination of the full assemblage of particles revealed that the top 20% of particles based on rank abundance (hereafter referred to as common particles) represented 98.9% of the total number of particles. Of these twenty-nine common particle types, sixteen were single-element particles while the remainder had either two or three elements (Figure 3). Except for cadmium (Cd) and lanthanum (La), all other elements considered for this study were present in the common particle pool (Figure 3). The thirteen common multi-element particles had either two or three elements per particle and typically consisted of Fe and/or Mn associated with Al, Pb, U, Ti, Cu, Ni, and/or Si. Elements found as common single-element particles but not in common multi-element particles included Ba, Zn, V, As, W, Au, and Ce.

Both Fe and Mn were ubiquitous in single and multi-element particles as evidenced by the top three particle compositions by rank-abundance being Fe, Mn, and Mn-Fe (11,124 Fe, 3,917 Mn, and 3,326 Mn-Fe particles). Single and multi-element particles containing Fe and Mn with and without other elements comprised 82% of all particles detected. Though both Fe and Mn were ubiquitous, Fe was in 65% and Mn in 31% of common particles. In addition to their importance in common particles, Fe and Mn were also abundant in rare particles, where they were present in 79% of the 263 rare particles detected.

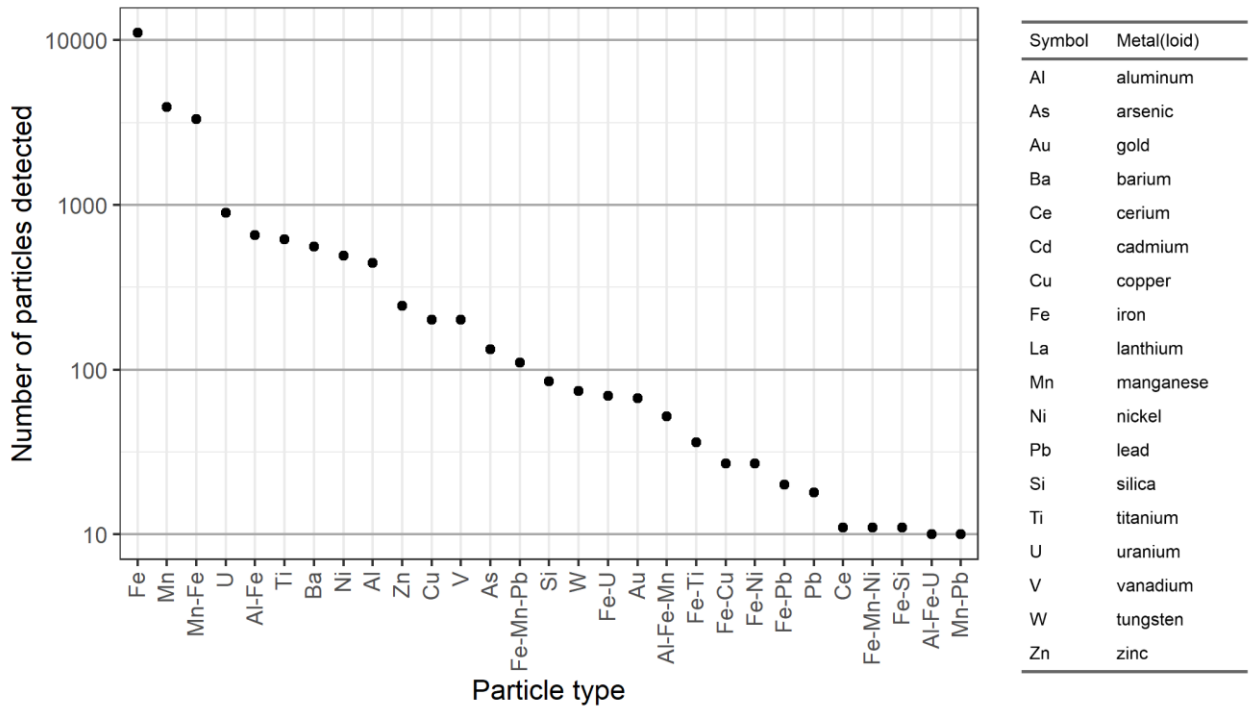


Figure 3: Rank abundance of common particle types across all ten sites and all elements by symbol considered for this study. The order of the elements in a particle type is indicative of their relative abundance in that particle type.

*Number of moles per particle*

For the sixteen elements detected as single-element particles, the median particles were in the range of 1 to 1000 amol particle$^{-1}$ (1 amol = $10^{-18}$ mol; Figure 4A), though the 95% confidence interval of the median around most particles was small. The five heaviest elements (i.e., U, W, Pb, Au, and Ce) had the smallest median values, in the 1 to 10 amol particle$^{-1}$ range. The lighter transition metals (i.e., Fe, Mn, Ni, Zn, Cu, and V) as well as Al, As, and Ba in single-element particles had medians between 10 and 100 amol particle$^{-1}$. There were only two elements with medians in the 100 to 1000 amol particle$^{-1}$ range, namely Ti and Si with 124 and 544 amol particle$^{-1}$, respectively. For the most part, the confidence intervals around the median value for most particle types were fairly small, and the difference between the upper and lower confidence intervals was less than 6% for many single-element particles (see Appendix C for median and

confidence interval tables) However, the range in moles per particle was sometimes large. This was most noticeable for Fe in common particles, which had a maximum number of moles per particle that was between two and five-hundred-fold larger than the minimum value for that some particle types.

When found in common multi-element particles, the median number of moles of Fe, Mn, or both, was often greater than for other elements like Al, Cu, and Pb. For example, moles of Fe and Mn were more than thirty-fold higher than Pb in Fe-Pb and Fe-Mn-Pb particles. Similarly, there was sixteen-fold more moles of Mn than Pb in Mn-Pb, and the median moles of Fe were six-fold greater than Cu in Fe-Cu. Exceptions to this trend include Ti-Fe and Si-Fe, where there was a bigger disparity and the medians of Ti and Si were over two-fold and five-fold higher than Fe, respectively. Of a total of thirteen common multi-element particles, Fe had a higher median in eight out of twelve particle types, and for Mn, it was true in three out of five (Figure 4B, C). When comparing Fe and Mn to one another in common multielement particles, their relative abundance varied by particle type. While Mn had a slightly higher median number of moles for Mn-Fe and Mn-Fe-Pb particles, Fe had a much higher median number of moles in Fe-Mn-Al and Fe-Mn-Ni particles.

Many elements had similar median numbers of moles per particle in both single and multi-element particles, with the exception of both Fe and Mn. When Pb, Cu, Si, and Ti were in multi-element particles, the median number of moles of those elements was no more than 20% greater than when they were in single-element particles. In the case of Pb, the median was 10% lower when found as Mn-Pb particles than in single-element form. For U, Ni, and Al, the median number of moles of those elements in multi-element particles was between 48 and 65% larger than when in single-element particles. For Fe and Mn, however, differences were much larger.

For example, Mn in Mn-Fe-Pb particles was five-fold larger than in Mn particles, while Fe in Fe-Mn-Ni particles was 76-fold larger than in Fe particles.

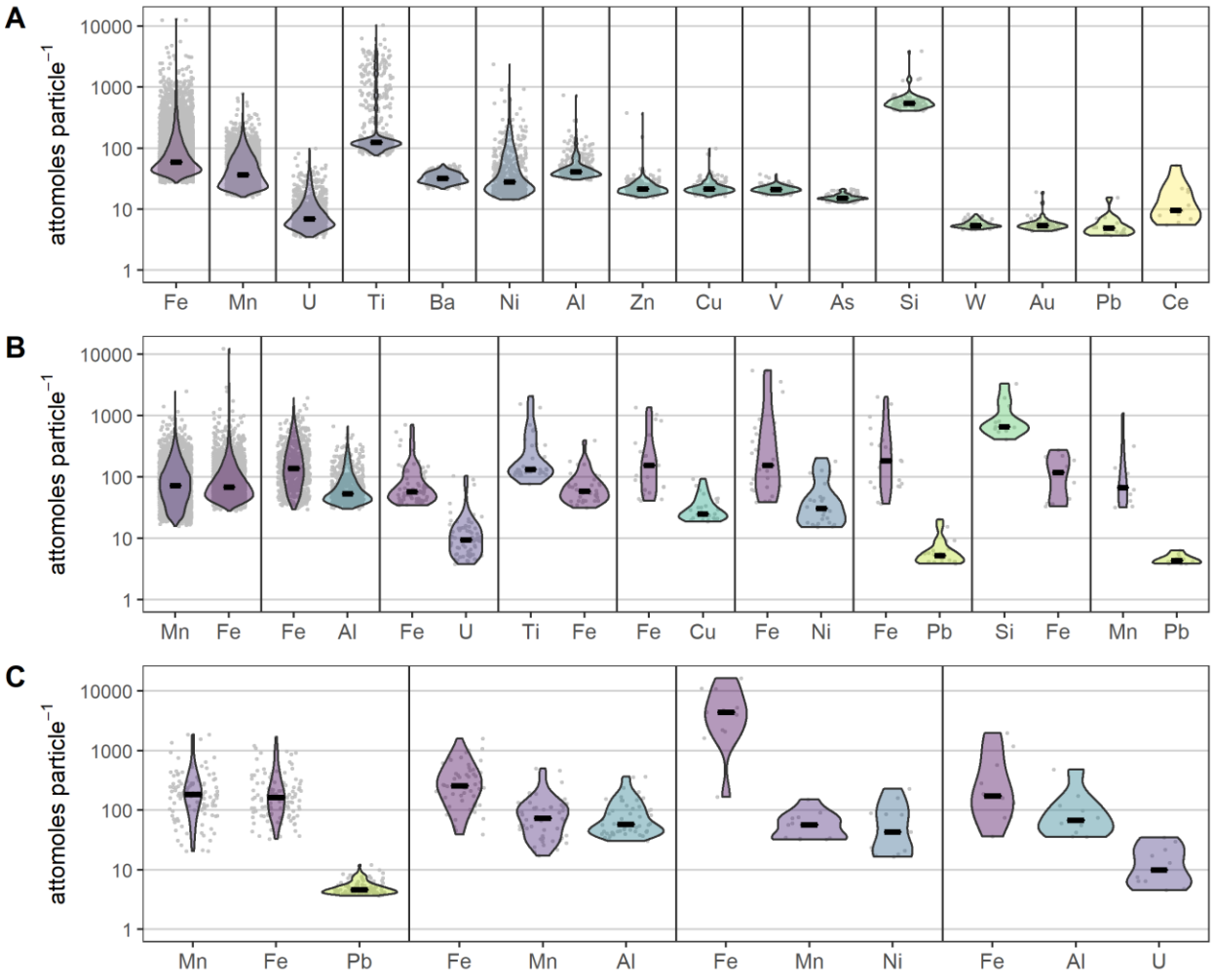


Figure 4: Violin plots of the number of moles per particle for each common particle type grouped by (A) single-element (B) two-element and (C) three-element particles. Elements in multi-element particles are ordered by decreasing median values within particles. Particles are ordered from most to least abundant by number within each panel. The solid vertical lines delineate between different particle types, gray dots are individual data points, and short black horizontal indicate median values.

### 3.2.2 Size of metal oxide particles

For the subset of particle types for which we calculated particle size, we found that most single-element particle types had median sizes in the nanoparticle range (1 to 100 nm), all two-element

particle types had median sizes in the 75 to 170 nm range, and all three-element particle types had median sizes in the 130 to 380 size range. For single-element particles, the median particle size of Fe was 88.0 ± 14.6 nm (median ± median absolute deviation), Mn was 61.3 ± 12.2 nm, and Al was 67.2 ± 4.5 nm. While these three were all fairly close to one another, Si particles were roughly two-fold larger (133 ± 8.1 nm; Figure 5A). When averaging across all four of these single-element particles, the median size was 82.6 ± 51.1 nm (Figure 5B).

Most two-element particles had median sizes either in the nanoparticle range or just above. The median sizes of Mn-Pb (74.9 ± 22.5 nm), Fe-U (87.0 ± 13.6 nm), and Fe-Ti (87.8 ± 14.3 nm) were all in the nanoparticle size range and of the same order of magnitude as single-element Fe, Mn, and Al. All other two-element particles were just above the nanoparticle range with medians that ranged from 109.9 ± 19.2 nm for Mn-Fe to 166 ± 31.9 nm for Fe-Si. Overall, the median size for two-element particles was 111.2 ± 21.9 nm.

Three-element particle types had both the largest median values and the largest ranges of median values. The smallest three-element particle type was Al-Fe-U, which was 135 ± 41.4 nm, which was larger than the median for all single element particles and all but one two-element particle type, namely Fe-Si. Particles of Fe-Mn-Ni were the largest of the three-element particles with a median diameter value of 373 ± 124 nm.

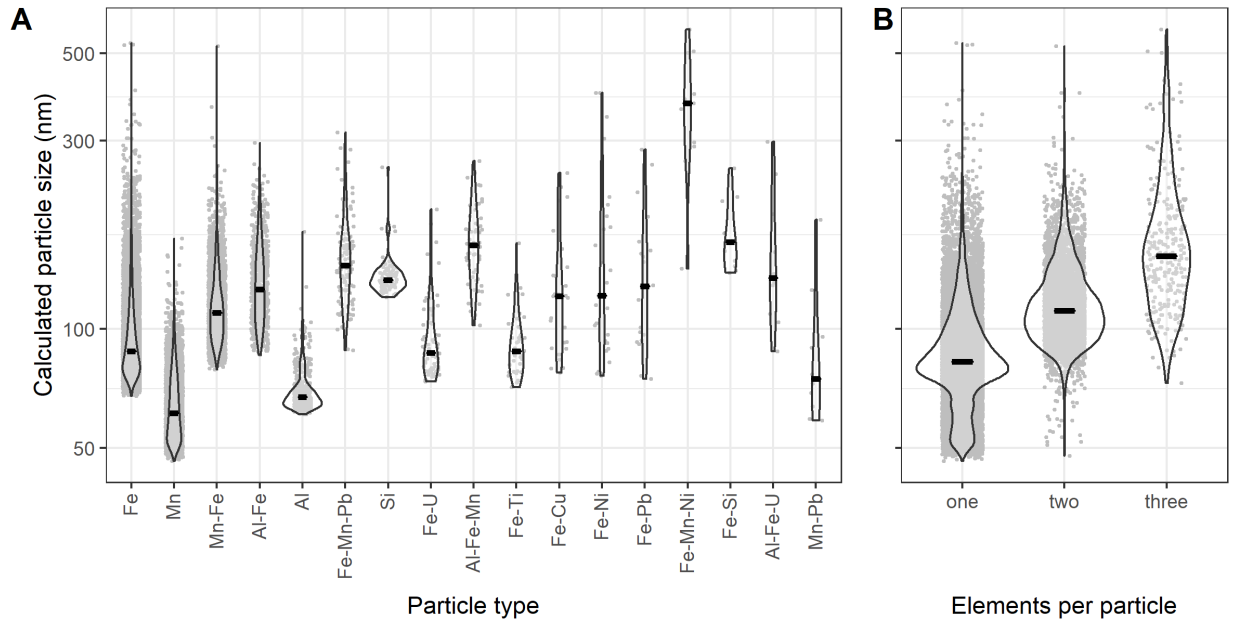


Figure 5: Violin plots of the particle size of common metal oxide particles by (A) particle type and (B) number of elements per particle. The x-axis on panel A is ordered from most to least common particles and the gray points represent individual particles.

## 3.3 Spatial Patterns

### 3.3.1 Longitudinal abundance, concentration, and load of particle types

Consistent with the patterns observed across all sites, single-element Fe particles were the most abundant at every site, followed by Mn and Mn-Fe at most mainstem UCFR sites and other single-element particles at the two tributaries (Figure 6). The number of Fe particles was greater than Mn at all sites and two-fold greater or more at CF5 and sites downstream. There were over twenty-fold more Fe than Mn particles at downstream tributary LB, a difference much greater than other sites. Up through CF4, Mn and Mn-Fe were the next most abundant particle types. For example, at CF3 42% of all detected particles were Fe-particles, while 21% were Mn, and 20% were Mn-Fe. Given that no other particle types were as abundant as these, we examined both the sum of the abundances of all remaining single-element particles and the sum of all remaining multi-element particles, which at CF3 represented 13% and 3.7% of all particles, respectively.

From CF5 downstream, the relative amount of other single-element particles was greater than or similar to Mn and Mn-Fe, however all three categories were less than Fe. The clearest example of this pattern was at LB, where the Mn-particles were 2.9% Mn-Fe represented 3.0 % relative to a high number of Fe (69%), other single (18%), and other multi-element particles (7.2%).

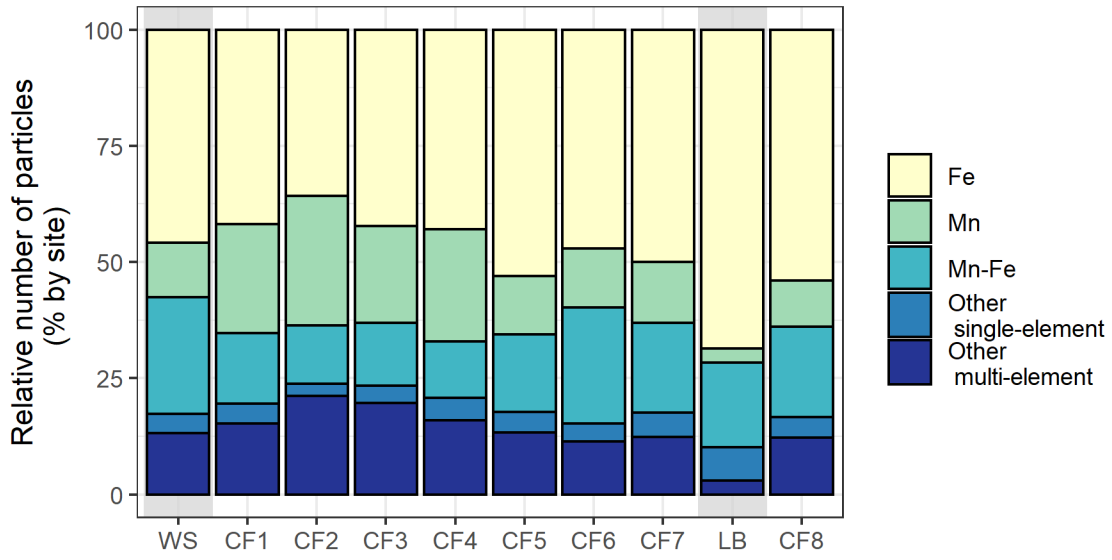


Figure 6: The longitudinal change in the relative number of particles binned as single-element Fe, single-element Mn, two-element Mn-Fe, all other single-element, and all other multi-element particles along the CF and two tributaries. The total number of particles at each site equals 100% on the y-axis.

There was a correlation between the particle concentrations (number of particles per L) of Mn and Mn-Fe, which stands in contrast to the much weaker correlation between Fe and Mn-Fe particles (Figure 7). The concentrations of Mn and Mn-Fe (Figure 7) were closely related among the study sites, yielding a Pearson's r of 0.91 ($p < 0.0001$), while Fe and Mn-Fe particles had a much lower Pearson's r of 0.29 ($p = 0.12$). There was a tighter relationship between Fe particles and both Mn-Fe and Mn particles from sites CF1 through CF4, as the pattern diverged starting at CF5 where both Mn and Mn-Fe particles decreased, while the concentration of Fe stayed fairly constant.

There was a general increase in particle load over the first seven UCFR sites, and the load either remained steady or decreased following the tributary inputs at LB. The particle load (number of particles per unit time) of Fe and other single and multi-element particles increased from CF1 to CF7, while the Mn and Mn-Fe particle load declined at CF5 before Mn-Fe increased again and Mn remained steady. The Fe particle load was similar at CF8 as CF7, despite the substantial inputs of Fe from LB that were one-third the load upstream of the confluence at CF7. Aligning with patterns in Fe, all other single and multi-element particles were similar in particle load at CF7 and CF8 save Mn and Mn-Fe, which decreased between CF7 and CF8. However, unlike Fe, the Mn inputs from LB were small and only a fraction of the CF7 load (Figure 7).

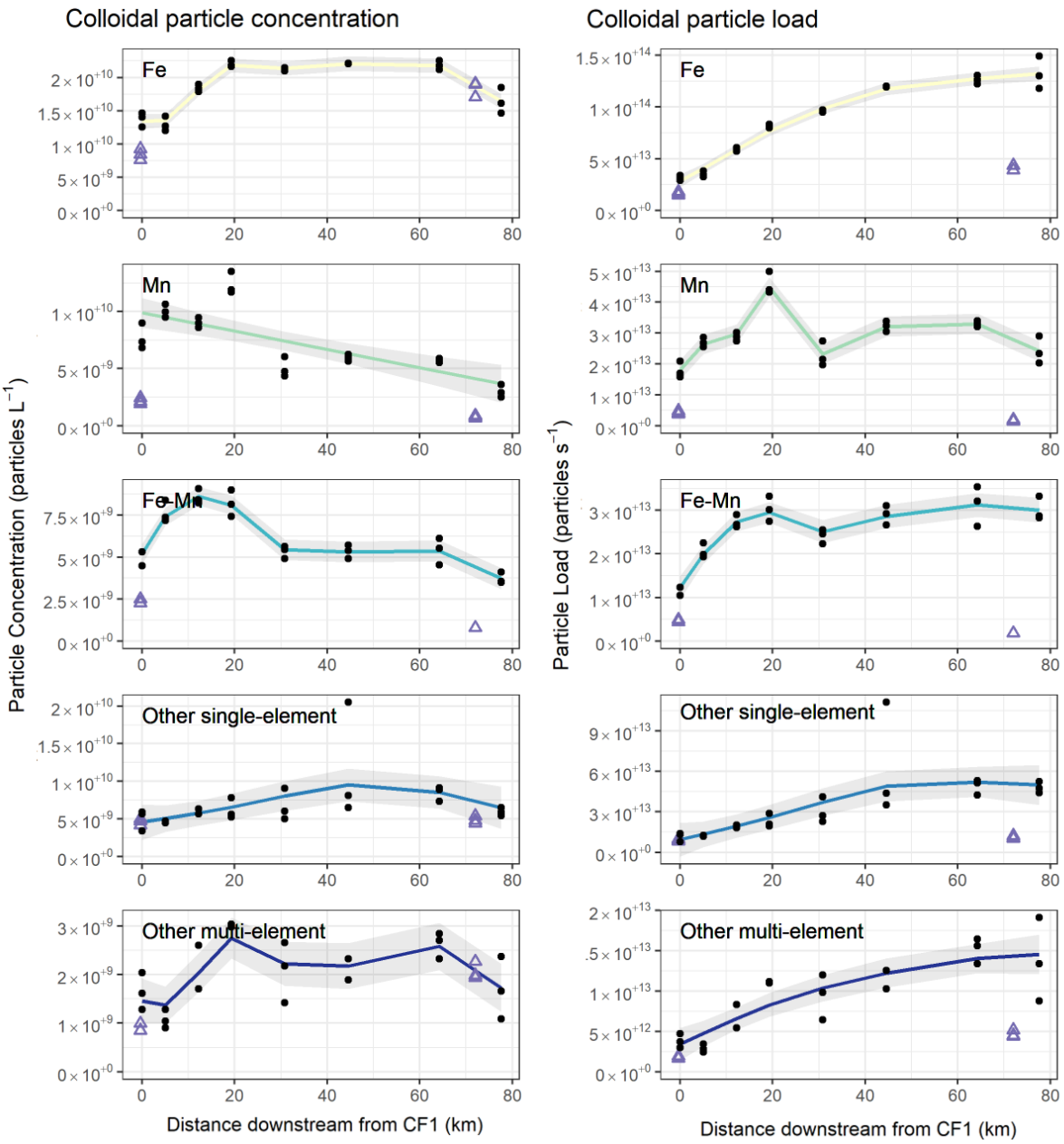


Figure 7: Longitudinal change in particle concentration (left) and load (right) along the CF. The two tributaries are described by purple triangles and presented on the figure for visual comparison, however, were not included in the generalized additive models of concentration and load. The gray ribbons represent the 95% confidence interval of the model, and the points are data used to produce the model. The particles are binned the same as Figure 6. Deviance in particle concentrations explained by generalized additive models using site as a predictor included: Fe (93%), Mn (52%), Fe-Mn (90%), other single-element (28%), and other multi-element (57%). Deviance in particle loads explained by generalized additive models using site as a predictor included: Fe (97%), Mn (88%), Fe-Mn (86%), other

single-element (55%), and other multi-element (72%). P-values for the smooth terms of each model are found in Appendix C, Table 8.

### 3.3.2 Longitudinal concentration and load of elements

For many elements measured as colloidal particles in samples from the mainstem of the Clark Fork, there was an overall increase in their mass concentration moving from upstream to downstream, though several varied along the reach (Figure 8A). For example, colloidal Fe increased from the first site, CF1 (146 ± 19 µg/L; mean ± SE) to CF4 at 19-km downstream (213 ± 14 µg/L). After CF4, the concentration of colloidal Fe then remained steady to CF7 at 64-km downstream from CF1. Colloidal Mn similarly increased from CF1 (56 ± 5.8 µg/L) to CF4 (96 ± 5.5 µg/L), however consistent with the number concentration of Mn and Mn-Fe particles, it decreased at CF5 and remained depressed in concentration. Colloidal Cu, Zn, As, and Pb all showed a pattern similar to Fe, increasing from upstream to downstream between CF1 and CF4 before remaining steady until CF7.

Much like with particle loads, the colloidal-mass load for many elements increased over the first seven mainstem sites, with the exception of Mn which peaked at CF4 (Figure 8B). Colloidal Fe increased in load by more than three-fold between CF1 and CF7, while colloidal Zn and As increased four-fold over the same sites. The increased loads of colloidal Cu and Pb were even more pronounced at more than thirteen-fold greater at CF7 than at CF1. In contrast, colloidal Mn increased by three-fold from CF1 to CF4 before decreasing by 40% at CF5, after which the load remained steady CF7.

Inputs from the tributary LB contributed to an increase in the colloidal load for some elements between CF7 and CF8, though the loads for many colloidal elements decreased between the two sites (Figure 8B). The load for colloidal forms of Zn and Cu both increased from CF7 to CF8,

despite small colloidal particle inputs from LB. For Zn, the colloidal load increased from 4.7 ± 0.49 mg $s^{-1}$ at CF7 to 9.8 ± 0.52 mg $s^{-1}$ at CF8, despite LB being less than 2 mg $s^{-1}$. The pattern in colloidal Cu was similar, and the load increased from 6.9 ± 0.40 mg $s^{-1}$ at C7 to 8.0 ± 0.51 mg $s^{-1}$ at CF8. Mn showed the opposite pattern, where the colloidal Mn load decreased from 298 ± 21.9 mg $s^{-1}$ at CF7 to 213 ± 22.2 mg $s^{-1}$ at CF8, despite a small Mn input from LB. Like Mn, the loads of colloidal As and Pb decreased between CF7 and CF8. Finally, despite the load of colloidal Fe particles from LB being approximately one-third that of CF7 (1349 ± 77.9 mg $s^{-1}$), the load of colloidal Fe at CF8 (1403 ± 104 mg $s^{-1}$) was similar to CF7 and stayed essentially unchanged from upstream to downstream of the confluence.

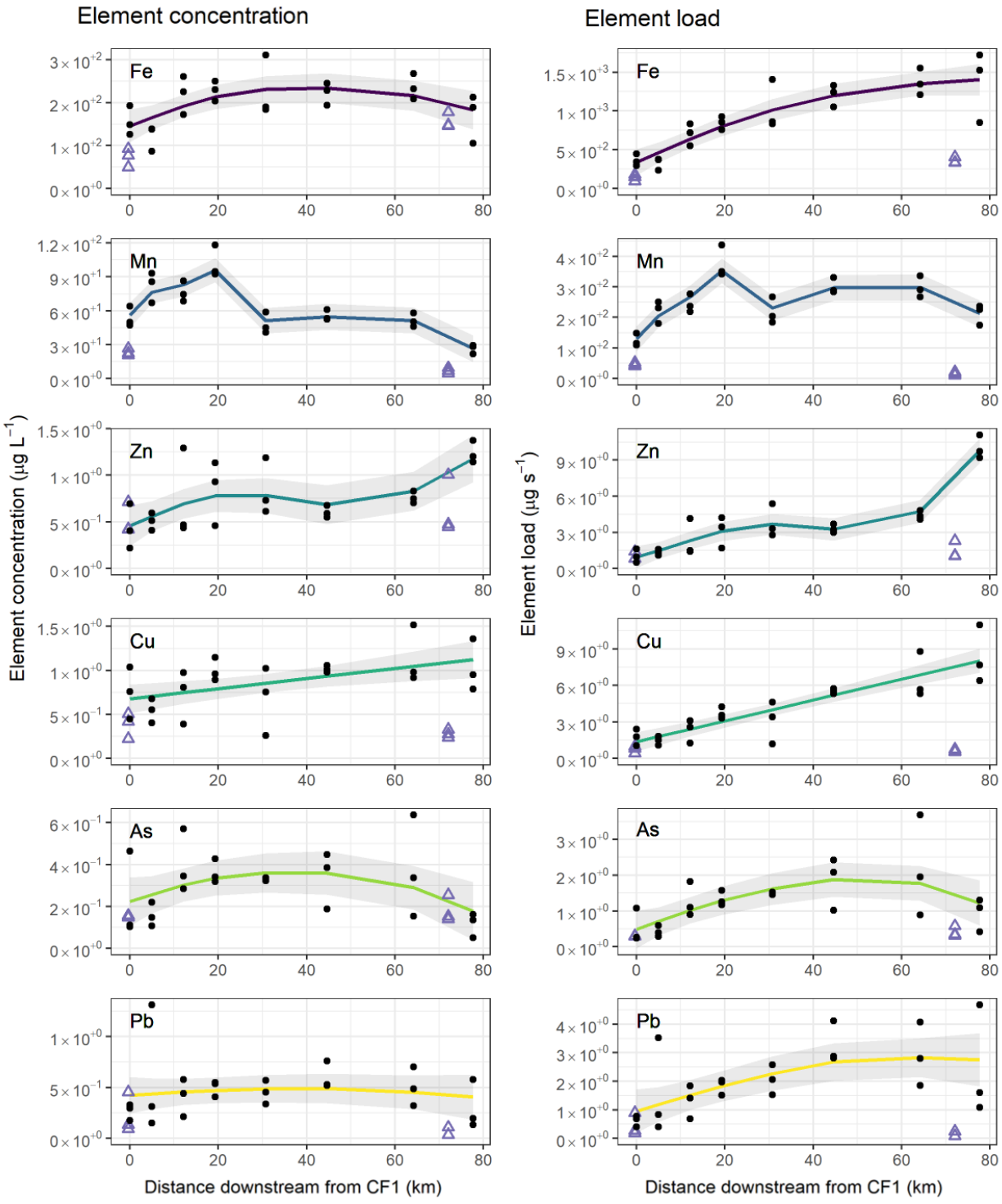


Figure 8: Longitudinal element mass (A) concentration and (B) load for colloidal forms of the elements Fe, Mn, Zn, Cu, As, and Pb along the Upper Clark Fork River. Elements are ordered from most to least numerically abundant moving from dark colors in the upper panels (Fe) to lighter colors in the bottom (Pb). The two tributaries are described by purple triangles and presented on the figure for visual

comparison, however, were not included in the generalized additive models of concentration and load. The gray areas represent the 95% confidence interval of the model, and the points are data used to produce the model. Deviance in element concentrations explained by generalized additive models using site as a predictor included: Fe (39%), Mn (81%), Zn (43%), Cu (23%), As (18%), Pb (-1%). Deviance in element loads explained by generalized additive models using site as a predictor included: Fe (78%), Mn (76%), Zn (89%), Cu (78%), As (38%), Pb (33%). P-values for the smooth terms of each model are found in Appendix C, Table 10.

# 4. Discussion

In this study, we used single particle inductively coupled plasma time-of-flight mass spectrometry (spICP-TOFMS) to characterize colloidal particles in the surface waters of the river, building on extensive previous work on metals in the UCFR that used other approaches. Our goal was to characterize the composition, size, and quantity of metal(loid) particles in the water column of this mine-waste contaminated river on a quantitative particle-by-particle basis to contribute to our understanding of metal exposure to organisms. We found a variety of elements in colloidal particles, with Fe and Mn as the most dominant elements. While we found evidence of particles consisting of multiple detected elements, single-element particles were dominant by both number and by mass. This information is complementary to findings from studies carried out using both single particle characterization through electron microscopy and bulk characterization methods such as X-ray diffraction, cascade filtration, and particle separation methods like field flow fractionation coupled to ICP-MS.

Though most particles detected by spICP-TOFMS consisted of a single element, we suggest that this method likely underestimates the occurrence and complexity of multi-element particles. The detection limits for spICP-TOFMS vary be element, but they are generally high enough that small particles may be missed, as will low masses of elements within particles (see Appendix C

for detection limits). For example, in the violin plots of attomoles of element per particle (Figure 4), it is evident that many elements have kernel density distributions that are truncated on the low end. This truncation is especially evident for contaminant elements Zn, Cu, As, and Pb when they are found as single-element particles. It is possible that particles that we detected as single-element particles of Zn, Cu, As, and Pb may have other elements associated with them that are below detection limit. Similarly, the abundant Fe, Mn, and Mn-Fe particles may also have appreciable amounts of Zn, Cu, As, or Pb associated with them, but not enough for that constituent to be detected. As such, this study provides conservative estimates of the concentrations of elements in the colloidal particle fraction. This study also likely overestimates the size of particles in the colloidal fraction by not capturing the smallest particles in the sample.

### 4.1 Nanoparticles and larger colloidal particles may be contaminant vectors

Many of the colloidal particles observed in this study were in or near the nanoparticle size range (1 to 100 nm), and work on engineered nanoparticles suggests that these particles may be an important form of metal/metalloid exposure to consider in the UCFR. For example, Fe, Mn, and Al particles were typically below 100 nm, while Si particles were larger yet still close to the nanoparticle size range. Many multi-element particles were also under or near 100 nm, including Mn-Fe, Fe-Cu, and Fe-Pb. While little is known about the interactions of organisms with natural and incidental nanoparticles and colloidal particles, manufactured nanoparticles in aquatic ecosystems are accumulated by organisms (Yuan et al. 2018; Desmau et al. 2020) and metals and arsenic can be transferred by trophic pathways within aquatic ecosystems and between aquatic and terrestrial ecosystems (Langner et al. 2012; Mogren et al. 2013). Manufactured nanoparticles can be detrimental to aquatic life (Griffitt et al. 2008), even in low concentration chronic exposures (Zhu, Chang, and Chen 2010). It is thus likely that they natural and incidentally

formed nanoparticles and colloidal particles enter food webs through both aqueous and dietary exposure routes (Cain, Croteau, and Luoma 2011).

Particles observed in this study consisting primarily of Fe, Mn, Ti, and Si serve as potential vectors for the transport of other elements and exposure to organisms given our observations of their association with toxic elements and their inherent surface reactivity that is known to bind trace quantities of elements. Though our data likely underestimate the amount of toxic metal(loid)s associated with colloidal particles, there is strong evidence that Fe, Mn, Ti, and Si were associated with a variety of other elements in particles. In particles containing multiple elements, there were typically a greater number of moles of Fe, Mn, Ti, and Si present suggesting their role as vectors for other elements within particles. While Ti and Si were only observed as vectors for Fe, Fe and Mn were found associated with a variety of elements. Particles with Fe or Mn at the surface are highly sorptive for other metal(loid)s (Huang and Zhang 2020; Hassellöv and von der Kammer 2008). The role of Fe and Mn as vectors for other elements in the UCFR is consistent with literature evidence for their role as vectors in the sediment of the UCFR (Hochella et al. 2005). Given the abundance and composition of nano- and colloidal particles and that they can contribute to both aquatic and dietary exposure, it is likely these particles play a role in driving the accumulation of metal contaminants into periphyton and other aquatic organisms.

### 4.2 Biogeochemistry was a driver of colloidal particle composition

The dominance of Fe and Mn and comparative rarity of Al, Si, or Al-Si suggest biogeochemistry, not the resuspension of bed sediments, was driving the composition and concentration of the colloidal particle fraction at the time of sampling. If the resuspension of bed sediments were the dominant driver of the colloidal particle load, we would have expected to see more Al in the

colloidal fraction. We measured 7 to 18-fold more particles containing Fe than Al and 25 to 60-fold greater concentrations of Fe than Al in colloidal particles (see Appendix C). Similarly, there were 32 to 276-fold more particles with Fe than Si and 12 to 64-fold more Fe by concentration. In contrast, though Fe is still dominant in UCFR sediments, Fe is present at quantities that are only ~2-fold greater than Si and Al (Plathe et al. 2013).

The increase in the numeric and mass loads of particles along the UCFR suggests that particles are being produced throughout the watershed, though the mechanism is unclear. The redox activity of Fe and Mn in sediments and the stream channel may be why they are so ubiquitous as colloidal particles in the water column of the UCFR. For example, Fe and Mn are likely to be released as dissolved solutes in anoxic groundwater and hyporheic sediments (Ratié et al. 2019; McCarthy and Zachara 1989). Upon interacting with oxygen-rich surface waters, both Fe and Mn can be oxidized by biotic and abiotic processes forming insoluble oxides and oxyhydroxides (Huang and Zhang 2020). It is also possible that particle formation due to redox or pH driven phenomena may occur on or in the periphyton, and particles may then be released into the water column (Desmau et al. 2020). Additionally, a range of trace elements sorb onto iron and manganese-rich sediments (Hassellöv and von der Kammer 2008) and colloidal particles (Plathe et al. 2013; Yang et al. 2015). It is also possible that metal(loid)s found as truly dissolved solutes or as suspended particulate matter may be subsequently converted to colloidal particles (Fox 1988). Thus, the biogeochemical cycling of Fe and Mn from groundwater and sediments could be an important source of colloidal Fe and Mn in the water column as well as any metals or metalloids they sorb.

Decreases in the load of several elements in the colloidal fraction mid-way down the reach and non-additive loads between the UCFR and Little Blackfoot River suggest that there are also

important removal pathways for these colloidal particles and that their source terms may vary longitudinally. Consistent with work on particulate organic matter and sediment, it is likely that natural nanoparticles and larger colloidal particles are removed from the water column by a variety of biological and abiotic processes. While these particles are small enough that they are unlikely to settle out, filter feeding aquatic invertebrates can remove colloidal organic matter (Weltens, Goossens, and Van Puymbroeck 2000; Wotton 1996). Biofilms are efficient at removing nanoparticles from the water column (Desmau et al. 2020). It is also likely that colloidal particles would be removed as surface water moves through hyporheic flowpaths, either through sorption on microbial biofilms or through entrainment in pores (Feris et al. 2009).

## 5. Summary

In this study, we have shown that colloidal metal(loid) particles were abundant under baseflow conditions in a mine-waste contaminated river. By using spICP-TOFMS, we were able to quantify the number concentration of particles and the concentration of elements within each individual colloidal particle, a level of specificity not previously available due to instrument limitations. Our data revealed that the majority of detected particles were nanoparticles, which has implications for our understanding of the forms of metal(loid)s to which aquatic organisms are exposed. Our observation of abundant Fe, Mn, and Mn-Fe particles associated with other metal(loid)s confirmed our hypothesis and suggests there is a high probability that these two elements may act as vectors in the transport and exposure of organisms to potentially more harmful metal(loid)s. The patterns we observed in nano- and colloidal particle loads showed that there is biogeochemical cycling for these particles and provide evidence for upstream to

downstream accumulation and removal of particles from the water column, observations that warrant further investigation.

# 6. References


Aiken, George R., Heileen Hsu-Kim, and Joseph N. Ryan. 2011. "Influence of Dissolved Organic Matter on the Environmental Fate of Metals, Nanoparticles, and Colloids." *Environmental Science and Technology* 45 (8): 3196–3201. https://doi.org/10.1021/es103992s.

Bone, Audrey J., Jason M. Unrine, Benjamin P. Colman, Andreas P. Gondikas, and Cole W. Matson. 2012. "Biotic and Abiotic Interactions in Aquatic Microcosms Determine Fate and Toxicity of Ag Nanoparticles. Part 1. Aggregation and Dissolution." *Environmental Science and Technology* 46 (13): 6915–24. https://doi.org/10.1021/es204682q.

Brooks, David. 2015. "Remove the Dam, Restore the River." *Montana: The Magazine of Western History* 65 (3): 3–24.

Cadmus, Pete, Helena Guasch, Adam T. Herdrich, Berta Bonet, Gemma Urrea, and William H. Clements. 2018. "Structural and Functional Responses of Periphyton and Macroinvertebrate Communities to Ferric Fe, Cu, and Zn in Stream Mesocosms." *Environmental Toxicology and Chemistry* 37 (5): 1320–29. https://doi.org/10.1002/etc.4070.

Cain, Daniel J., Marie Noële Croteau, and Christopher C. Fuller. 2013. "Dietary Bioavailability of Cu Adsorbed to Colloidal Hydrous Ferric Oxide." *Environmental Science and Technology* 47 (6): 2869–76. https://doi.org/10.1021/es3044856.

Cain, Daniel J., Marie Noële Croteau, and Samuel Luoma. 2011. "Bioaccumulation Dynamics and Exposure Routes of Cd and Cu among Species of Aquatic Mayflies." *Environmental Toxicology and Chemistry* 30 (11): 2532–41. https://doi.org/10.1002/etc.663.

Colman, Benjamin P., Benjamin Espinasse, Curtis J. Richardson, Cole W. Matson, Gregory V. Lowry, Dana E. Hunt, Mark R. Wiesner, and Emily S. Bernhardt. 2014. "Emerging Contaminant or an Old Toxin in Disguise? Silver Nanoparticle Impacts on Ecosystems." *Environmental Science and Technology* 48 (9): 5229–36. https://doi.org/10.1021/es405454v.

Cook, N., T. Elam, J. Lindstrom, B. Liermann, and P. Saffel. 2017. "Fisheries Monitoring in the Upper Clark Fork River Basin 2017."

Croteau, Marie Noële, Agnieszka D. Dybowska, Samuel N. Luoma, and Eugenia Valsami-Jones. 2011. "A Novel Approach Reveals That Zinc Oxide Nanoparticles Are Bioavailable and Toxic after Dietary Exposures." *Nanotoxicology* 5 (1): 79–90. https://doi.org/10.3109/17435390.2010.501914.

Desmau, Morgane, Andrea Carboni, Maureen Le Bars, Emmanuel Doelsch, Marc F. Benedetti, Mélanie Auffan, Clément Levard, and Alexandre Gelabert. 2020. "How Microbial Biofilms

Control the Environmental Fate of Engineered Nanoparticles?" *Frontiers in Environmental Science* 8 (July). https://doi.org/10.3389/fenvs.2020.00082.

Farag, Aïda M., David A. Nimick, Briant A. Kimball, Stanley E. Church, David D. Harper, and William G. Brumbaugh. 2007. "Concentrations of Metals in Water, Sediment, Biofilm, Benthic Macroinvertebrates, and Fish in the Boulder River Watershed, Montana, and the Role of Colloids in Metal Uptake." *Archives of Environmental Contamination and Toxicology* 52 (3): 397–409. https://doi.org/10.1007/s00244-005-0021-z.

Feris, Kevin P., Philip W. Ramsey, Sean M. Gibbons, Chris Frazar, Matthias C. Rillig, Johnnie N. Moore, James E. Gannon, and William E. Holben. 2009. "Hyporheic Microbial Community Development Is a Sensitive Indicator of Metal Contamination." *Environmental Science and Technology* 43 (16): 6158–63. https://doi.org/10.1021/es9005465.

Fox, Lewis E. 1988. "The Solubility of Colloidal Ferric Hydroxide and Its Relevance to Iron Concentrations in River Water." *Geochimica et Cosmochimica Acta* 52 (3): 771–77. https://doi.org/10.1016/0016-7037(88)90337-7.

Griffitt, Robert J., Jing Luo, Jie Gao, Jean Claude Bonzongo, and David S. Barber. 2008. "Effects of Particle Composition and Species on Toxicity of Metallic Nanomaterials in Aquatic Organisms." *Environmental Toxicology and Chemistry* 27 (9): 1972–78. https://doi.org/10.1897/08-002.1.

Guéguen, C., and J Dominik. 2003. "Partitioning of Trace Metals between Particulate , Colloidal and Truly Dissolved Fractions in a Polluted River : The Upper Vistula River ( Poland )." *Applied Geochemistry* 18: 457–70.

Hassellöv, Martin, and Frank von der Kammer. 2008. "Iron Oxides as Geochemical Nanovectors for Metal Transport in Soil-River Systems." *Elements* 4 (6): 401–6. https://doi.org/10.2113/gselements.4.6.401.

Helgen, Steven O., and Andy Davis. 2000. "Quantifying Metal Contributions from Multiple Sources to the Clark Fork River, Montana, U.S.A." *Environmental Forensics* 1 (2): 55–62. https://doi.org/10.1006/enfo.2000.0008.

Hochella, Michael F., Takeshi Kasama, Andrew Putnis, Christine V. Putnis, and Johnnie N. Moore. 2005. "Environmentally Important, Poorly Crystalline Fe/Mn Hydrous Oxides: Ferrihydrite and a Possibly New Vernadite-like Mineral from the Clark Fork River Superfund Complex." *American Mineralogist* 90 (4): 718–24. https://doi.org/10.2138/am.2005.1591.

Hornberger, Michelle I, Samuel N Luoma, Michael L Johnson, Marcel Holyoak, S Geological Survey, Middlefield Rd, and Menlo Park. 2009. "Influence of Remediation in a Mine-Impacted River : Metal Trends over Large Spatial and Temporal Scales Author ( s ): Michelle I . Hornberger , Samuel N . Luoma , Michael L . Johnson and Marcel Published by : Wiley on Behalf of the Ecological Society of A" 19 (6): 1522–35.

Huang, Jianzhi, and Huichun Zhang. 2020. "Redox Reactions of Iron and Manganese Oxides in Complex Systems." *Frontiers of Environmental Science and Engineering* 14 (5). https://doi.org/10.1007/s11783-020-1255-8.

Kammer, Frank von der, Samuel Legros, Thilo Hofmann, Erik H. Larsen, and Katrin Loeschner. 2011. “Separation and Characterization of Nanoparticles in Complex Food and Environmental Samples by Field-Flow Fractionation.” *TrAC - Trends in Analytical Chemistry* 30 (3): 425–36. https://doi.org/10.1016/j.trac.2010.11.012.

Langner, Heiko W., Erick Greene, Robert Domenech, and Molly F. Staats. 2012. “Mercury and Other Mining-Related Contaminants in Ospreys along the Upper Clark Fork River, Montana, USA.” *Archives of Environmental Contamination and Toxicology* 62 (4): 681–95. https://doi.org/10.1007/s00244-011-9732-5.

McCarthy, John F., and John M. Zachara. 1989. “Subsurface Transport of Contaminants.” *Environmental Science & Technology* 23 (5): 496–502.

Mogren, Christina L., William E. Walton, David R. Parker, and John T. Trumble. 2013. “Trophic Transfer of Arsenic from an Aquatic Insect to Terrestrial Insect Predators.” *PLoS ONE* 8 (6): 2–7. https://doi.org/10.1371/journal.pone.0067817.

Montaño, Manuel D., Frank von der Kammer, Chad W. Cuss, and James F. Ranville. 2019. “Opportunities for Examining the Natural Nanogeochemical Environment Using Recent Advances in Nanoparticle Analysis.” *Journal of Analytical Atomic Spectrometry* 34 (9): 1768–72. https://doi.org/10.1039/c9ja00168a.

Moore, Johnnie N., and Heiko W. Langner. 2012. “Can a River Heal Itself? Natural Attenuation of Metal Contamination in River Sediment.” *Environmental Science and Technology* 46 (5): 2616–23. https://doi.org/10.1021/es203810j.

Naughton, J., M. Burke, S. Ellsworth, T. Traxler, W. Bollman, B. Kerans, N. Cook, T. Elam, and G. Swant. 2019. “Monitoring Report for 2018 Clark Fork River Operable Unit.”

Naughton, J., M. Burke, B. Merritt, T. Traxler, B. Kerans, W. Bollman, and G. Swant. 2020. “MONITORING REPORT FOR 2019 CLARK FORK RIVER OPERABLE UNIT.” https://deq.mt.gov/Portals/112/Land/FedSuperFund/Documents/cfr/Documents and Reports/CFR 2019 Monitoring Report.pdf?ver=2020-10-20-145945-583.

Nimick, David A., and Johnnie N. Moore. 1991. “Prediction of Water-Soluble Metal Concentrations in Fluvially Deposited Tailings Sediments, Upper Clark Fork Valley, Montana, U.S.A.” *Applied Geochemistry* 6 (6): 635–46. https://doi.org/10.1016/0883-2927(91)90074-Y.

NOAA. 2018. “Northwest River Forecast Center Monthly Precipitation Table.” 2018. https://www.nwrfc.noaa.gov/water_supply/wy_summary/wy_summary.php?tab=5.

NRCS. 2012. “USDA.” *Nutrition & Food Science* 42 (4): 11–14. https://doi.org/10.1108/nfs.2012.01742daa.005.

Paiva Magalhães, Danielly de, Mônica Regina da Costa Marques, Darcilio Fernandes Baptista, and Daniel Forsin Buss. 2015. “Metal Bioavailability and Toxicity in Freshwaters.” *Environmental Chemistry Letters* 13 (1): 69–87. https://doi.org/10.1007/s10311-015-0491-9.

Plathe, K. L., F. Von Der Kammer, M. Hassellöv, J. Moore, M. Murayama, T. Hofmann, and M. F. Hochella. 2010. “Using FlFFF and ATEM to Determine Trace Metalnanoparticle

Associations in Riverbed Sediment." *Environmental Chemistry* 7 (1): 82–93. https://doi.org/10.1071/EN09111.

Plathe, K. L., Frank von der Kammer, Martin Hassellöv, Johnnie N. Moore, Mitsuhiro Murayama, Thilo Hofmann, and Michael F. Hochella. 2013. "The Role of Nanominerals and Mineral Nanoparticles in the Transport of Toxic Trace Metals: Field-Flow Fractionation and Analytical TEM Analyses after Nanoparticle Isolation and Density Separation." *Geochimica et Cosmochimica Acta* 102: 213–25. https://doi.org/10.1016/j.gca.2012.10.029.

R. 2020. "R: A Language and Environment for Statistical Computing. R Foundation for Statistical Computing." Vienna, Austria. https://www.r-project.org/.

Ratié, GA, D Vantelon, I Lotfi Kalahroodi, E., Bihannic, A.C. Pierson-Wickmann, and M. Davranche. 2019. "Iron Speciation at the Riverbank Surface in Wetland and Potential Impact on the Mobility of Trace Metals." *Science of the Total Environment* 651: 443–55.

Scimeca, Manuel, Simone Bischetti, Harpreet Kaur Lamsira, Rita Bonfiglio, and Elena Bonanno. 2018. "Energy Dispersive X-Ray (EDX) Microanalysis: A Powerful Tool in Biomedical Research and Diagnosis." *European Journal of Histochemistry* 62 (1): 89–99. https://doi.org/10.4081/ejh.2018.2841.

Sigg, Laura, Hanbin Xue, David Kistler, and René Sshönenberger. 2000. "Size Fractionation (Dissolved, Colloidal and Particulate) of Trace Metals in the Thur River, Switzerland." *Aquatic Geochemistry* 6 (4): 413–34. https://doi.org/10.1023/A:1009692919804.

Stolpe, Björn, Laodong Guo, Alan M. Shiller, and George R. Aiken. 2013. "Abundance, Size Distributions and Trace-Element Binding of Organic and Iron-Rich Nanocolloids in Alaskan Rivers, as Revealed by Field-Flow Fractionation and ICP-MS." *Geochimica et Cosmochimica Acta* 105: 221–39. https://doi.org/10.1016/j.gca.2012.11.018.

Sullivan, Lauren. 2019. "Colloidal and Truly Dissolved Metal (Loid)s in Wastewater Lagoons and Their Removal with Floating Treatment Wetlands." *Graduate Student Theses, Dissertations, & Professional Papers*.

Trostle, Kyle D., J. Ray Runyon, Michael A. Pohlmann, Shelby E. Redfield, Jon Pelletier, Jennifer McIntosh, and Jon Chorover. 2016. "Water Resources Research." *Journal of the American Water Resources Association* 52: 7931–44. https://doi.org/10.1111/j.1752-1688.1969.tb04897.x.

US Environmental Protection Agency. 2004. "Record of Decision Summary." https://deq.mt.gov/Portals/112/Land/FedSuperFund/Documents/cfr/Documents and Reports/ROD/1_RODDecisionSummary.pdf?ver=2018-04-18-165717-587&timestamp=1524092689084.

Weltens, R., R. Goossens, and S. Van Puymbroeck. 2000. "Ecotoxicity of Contaminated Suspended Solids for Filter Feeders (Daphnia Magna)." *Archives of Environmental Contamination and Toxicology* 39 (3): 315–23. https://doi.org/10.1007/s002440010110.

Wilhelm, Linda, Katharina Besemer, Christina Fasching, Tim Urich, Gabriel A. Singer, Christopher Quince, and Tom J. Battin. 2014. "Rare but Active Taxa Contribute to

Community Dynamics of Benthic Biofilms in Glacier-Fed Streams." *Environmental Microbiology* 16 (8): 2514–24. https://doi.org/10.1111/1462-2920.12392.

Wood, Simon N. 2021. *Generalized Additive Models: An Introduction with R, Second Edition*. *Generalized Additive Models: An Introduction with R, Second Edition*. https://doi.org/10.1201/9781315370279.

Wotton, Robert S. 1996. "Colloids , Bubbles , and Aggregates : A Perspective on Their Role in Suspension Feeding." *Journal of the North American Benthological Society* 15 (1): 127–35.

Yang, Yi, Benjamin P. Colman, Emily S. Bernhardt, and Michael F. Hochella. 2015. "Importance of a Nanoscience Approach in the Understanding of Major Aqueous Contamination Scenarios: Case Study from a Recent Coal Ash Spill." *Environmental Science and Technology* 49 (6): 3375–82. https://doi.org/10.1021/es505662q.

Yuan, Lin, Curtis J. Richardson, Mengchi Ho, C. Wesley Willis, Benjamin P. Colman, and Mark R. Wiesner. 2018. "Stress Responses of Aquatic Plants to Silver Nanoparticles." *Environmental Science and Technology* 52 (5): 2558–65. https://doi.org/10.1021/acs.est.7b05837.

Zhu, Xiaoshan, Yung Chang, and Yongsheng Chen. 2010. "Toxicity and Bioaccumulation of TiO2 Nanoparticle Aggregates in Daphnia Magna." *Chemosphere* 78 (3): 209–15. https://doi.org/10.1016/j.chemosphere.2009.11.013.

# Appendix A. Data processing

Please contact author for project data and code.

## A.1 Calibration

$$\text{Mass flux slope} = \frac{\text{Intensity}}{\text{Au standard concentration} * \text{te} * \text{fr} * \text{dt} * 10^{-3}\ (\text{conversion})} \quad (1)$$

Where:

**Intensity (int)** is the intensity outputted by the standard

**Concentration (conc)** is the concentration of the gold standard of nanoparticles

**Transport efficiency (te)** accounts for incomplete transport of nanoparticles in suspension (relative to the complete transport of dissolved ions in solution)

**Flow rate (fr)** is the rate the sample flows through the system

**Dwell time (dt)** is the detection time, shorter dwell times can reduce background signal and allow us to analyze higher particle number concentrations

## A.2 Element mass

The mass of elements within particles was calculated by removing the background signal from the peak intensity signals that indicate particles. The peak intensities, or counts, were divided by the mass fraction and slope of the mass flux curve calculated in Equation (1). The mass fraction is a ratio of the mass of the element of interest to the rest of the elements. It is calculated based on assumptions about the form of metal assumed to be present in the river.

In calculating the mass of individual elements within particles, the particle is assumed to be by itself.

$$\text{element mass} = \frac{(\text{particle intensity} - \text{particle background}) * 10^{-6}\ (\text{dilution})}{\text{mass fraction} * \text{slope of mass flux curve}} * 1\ (\text{ionization eff.}) \quad (2)$$

## A.3 Discharge interpolation

The discharge was interpolated at sites CF1, CF3, CF4, CF5, and CF8 because USGS gauging stations were not available. These sites were interpolated as follows.

$$\text{discharge} = \text{some amalgam of the cfs at sites before and after scaled by river km distance between} \quad (3)$$

## A.4 Common particles

For the common particles, sum the number of particles in replicates A, B, and C by particle composition.

$$\text{Particle count} = \sum(\text{number of particles in replicate A, B, and C grouped by particle composition}) \quad (3)$$

Common particles were designated based on the 20% rule (see Methods).

$$\text{common particles} = 0.2 * n(\text{types of particles}) \quad (4)$$

## A.5 Number of moles per particle by element

$$\text{attomoles per particle } = \text{mass of element} * \frac{\text{moles of element}}{\text{mass of element}} * \frac{10^{18}\ \text{attomoles}}{\text{mole}} \quad (5)$$

## A.6 Oxide particle size

The element masses of Fe, Mn, Al, and Si are calculated under the assumption that they are present in an oxidized form. Assumptions are also based on prior research in the UCFR. These assumptions are: manganese dioxide ($MnO_2$), hematite ($Fe_2O_3$), aluminum oxide ($Al_2O_3$), and silicon dioxide ($SiO_2$).

$$\sum(\text{oxide mass values across particle compositions}) \quad (6)$$

Particle size is calculated using a density value using a density value of 2.65 g $cm^{-3}$ as it is a commonly assumed sediment density (NRCS, 2012).

$$\text{size } = \left(\frac{6\ *\ \text{oxide particle mass}}{\pi * \text{density } * 10^{-21}(\text{conversion})}\right) \quad (7)$$

## A.7 Mass concentration and load

Mass concentration

$$\text{mass concentration } = \frac{\text{mass } *\ 1000\ (\text{dilution factor}) *\ 10^6\ (\text{conversion})}{\text{transport efficiancy} *\ \text{flow rate } *\ \text{dwell time}} \quad (8)$$

Load

Guide for understanding mass and load

$$\text{load } \left(\frac{\text{g}}{\text{s}}\right) = \text{mass concentration } \left(\frac{\mu g}{L}\right) *\ \text{discharge } \left(\frac{ft^3}{s}\right) * \frac{28.32\ \text{L}}{ft^3} * \frac{1\ \text{g}}{1000\ \mu\text{g}} \quad (9)$$

## A.8 Particle concentration and load

$$\text{concentration } = \frac{\text{particle number } *\ 1000\ (\text{dilution factor})}{\text{te } *\ \text{fr } *\ \text{st}} \quad (10)$$

# Appendix B. Generalized Additive Modeling

To model the change in concentration and load over the river, a simple model was constructed to describe the system.

$$\text{concentration or load} \sim \text{smooth(site)} \quad (11)$$

The models were fitted with an appropriate smoothness parameter by using a restricted maximum likelihood approach (REML) for model selection.

# Appendix C. Tables

**Table 2. Site coordinates and corresponding USGS gages**

| Site | Name | Latitude | Longitude | Station Type | USGS Station |
|---|---|---|---|---|---|
| WS | Warm Springs Cr | 46.185918 | -112.773822 | tributary | 12323770 |
| CF1 | Warm Springs | 46.187207 | -112.7703 | UCFR | |
| CF2 | Perkins Rd | 46.208596 | -112.767602 | UCFR | 12324200 |
| CF3 | Galen Rd | 46.237429 | -112.753206 | UCFR | |
| CF4 | Racetrack | 46.265377 | -112.74468 | UCFR | |
| CF5 | Sager | 46.317384 | -112.736224 | UCFR | |
| CF6 | Deer Lodge | 46.383498 | -112.73798 | UCFR | 12324300 |
| CF7 | Kohrs Bend | 46.498017 | -112.741164 | UCFR | 12324300 |
| USGS | Above LB | 46.51091 | -112.789686 | USGS | 12324590 |
| LB | Little Blackfoot R | 46.51942 | -112.793396 | tributary | 12324590 |
| CF8 | DwnStrm from LBF | 46.519867 | -112.807675 | UCFR | |

**Table 3. Environmental data in order from most upstream (WS) to most downstream (CF8)**

| Site | Site Name | Time | Temp (°C) | pH | Dissolved Oxygen ($mgL^{-1}$) | SPC ($\mu SL^{-1}$) | Discharge ($m^3 s^{-1}$) |
|---|---|---|---|---|---|---|---|
| WS | Warm Springs Cr | 8:50 | 7.2 | 8.50 | 10.88 | 308.5 | 1.97 |
| CF1 | Warm Springs | 9:00 | 7.5 | 8.45 | 10.83 | 361.8 | 2.32 |
| CF2 | Perkins Rd | 9:10 | 7.7 | 8.62 | 10.58 | 369.6 | 2.69 |
| CF3 | Galen Rd | 9:25 | 7.8 | 8.68 | 10.94 | 433.0 | 3.19 |
| CF4 | Racetrack | 9:38 | 8.1 | 8.74 | 11.42 | 452.4 | 3.70 |
| CF5 | Sager | 9:50 | 8.2 | 8.71 | 10.94 | 448.2 | 4.53 |
| CF6 | Deer Lodge | 10:10 | 8.5 | 8.74 | 10.71 | 467.7 | 5.42 |
| CF7 | Kohrs Bend | 10:35 | 8.5 | 8.88 | 11.23 | 477.4 | 5.79 |
| LB | Little Blackfoot R | 10:53 | 8.6 | 8.72 | 10.92 | 296.7 | 2.29 |
| CF8 | DwnStrm from LBF | 11:03 | 8.5 | 8.84 | 11.57 | 430.0 | 8.08 |

**Table 4. Median number of attomoles per particle**

| Particle | Element | Median | CI Low | CI High | Min Value | Max Value | $\frac{Max}{Min}$ | $\frac{\text{CI Upper}}{\text{CI Lower}}$ |
|---|---|---|---|---|---|---|---|---|
| Fe | Fe | 59.04 | 58.77 | 59.77 | 26.79 | 13,030.19 | 486.38 | 1.02 |
| Mn | Mn | 36.75 | 36.40 | 37.95 | 15.84 | 776.35 | 49.01 | 1.04 |
| U | U | 7.00 | 6.92 | 7.32 | 3.46 | 98.44 | 28.45 | 1.06 |
| Ti | Ti | 124.39 | 123.25 | 126.66 | 75.82 | 10,474.19 | 138.15 | 1.03 |
| Ba | Ba | 31.98 | 31.70 | 32.84 | 21.47 | 54.33 | 2.53 | 1.04 |
| Ni | Ni | 27.89 | 27.21 | 30.24 | 14.37 | 2,365.21 | 164.59 | 1.11 |
| Al | Al | 41.31 | 40.88 | 42.21 | 30.54 | 744.65 | 24.38 | 1.03 |
| Zn | Zn | 21.40 | 21.05 | 21.95 | 15.43 | 380.32 | 24.65 | 1.04 |

| | | | | | | | | |
|---|---|---|---|---|---|---|---|---|
| Cu | Cu | 21.33 | 21.14 | 21.98 | 15.94 | 98.60 | 6.19 | 1.04 |
| V | V | 21.11 | 20.93 | 21.45 | 17.01 | 37.20 | 2.19 | 1.02 |
| As | As | 15.17 | 14.95 | 15.38 | 12.73 | 21.55 | 1.69 | 1.03 |
| Si | Si | 543.78 | 529.29 | 584.61 | 405.50 | 3,915.73 | 9.66 | 1.10 |
| W | W | 5.38 | 5.34 | 5.61 | 4.62 | 8.28 | 1.79 | 1.05 |
| Au | Au | 5.37 | 5.30 | 5.60 | 4.40 | 18.99 | 4.32 | 1.06 |
| Pb | Pb | 4.89 | 4.46 | 5.18 | 3.72 | 15.50 | 4.17 | 1.16 |
| Mn-Fe | Fe | 68.91 | 68.35 | 70.78 | 27.81 | 12,231.94 | 439.84 | 1.04 |
| Mn-Fe | Mn | 72.74 | 71.97 | 75.35 | 15.89 | 2,472.77 | 155.62 | 1.05 |
| Al-Fe | Fe | 136.86 | 131.30 | 148.81 | 29.71 | 1,943.16 | 65.40 | 1.13 |
| Al-Fe | Al | 53.44 | 52.30 | 55.49 | 29.92 | 662.89 | 22.16 | 1.06 |
| Fe-U | Fe | 57.16 | 56.07 | 69.38 | 34.78 | 706.49 | 20.31 | 1.24 |
| Fe-U | U | 9.47 | 8.97 | 11.80 | 3.81 | 103.33 | 27.12 | 1.32 |
| Fe-Ti | Fe | 58.69 | 54.48 | 74.28 | 31.36 | 389.81 | 12.43 | 1.36 |
| Fe-Ti | Ti | 131.76 | 128.00 | 200.20 | 76.22 | 2,063.73 | 27.08 | 1.56 |
| Fe-Cu | Fe | 155.05 | 105.25 | 219.99 | 40.55 | 1,339.61 | 33.04 | 2.09 |
| Fe-Cu | Cu | 25.08 | 24.15 | 32.14 | 18.61 | 92.86 | 4.99 | 1.33 |
| Fe-Ni | Fe | 155.45 | 125.35 | 500.20 | 38.46 | 5,419.00 | 140.90 | 3.99 |
| Fe-Ni | Ni | 30.77 | 27.64 | 42.51 | 15.29 | 202.54 | 13.25 | 1.54 |
| Fe-Pb | Fe | 183.02 | 89.34 | 324.52 | 36.40 | 2,003.68 | 55.05 | 3.63 |
| Fe-Pb | Pb | 5.22 | 4.46 | 5.75 | 3.85 | 20.29 | 5.27 | 1.29 |
| Fe-Si | Fe | 118.54 | 44.57 | 214.54 | 33.15 | 273.32 | 8.24 | 4.81 |
| Fe-Si | Si | 650.44 | 611.57 | 1,437.46 | 405.09 | 3,294.67 | 8.13 | 2.35 |
| Mn-Pb | Mn | 67.14 | 52.18 | 139.92 | 32.16 | 1,080.37 | 33.59 | 2.68 |
| Mn-Pb | Pb | 4.39 | 4.18 | 4.95 | 3.86 | 6.35 | 1.65 | 1.18 |
| Fe-Mn-Pb | Fe | 164.98 | 146.52 | 189.45 | 33.06 | 1,705.07 | 51.58 | 1.29 |
| Fe-Mn-Pb | Mn | 185.07 | 173.44 | 207.60 | 20.43 | 1,870.35 | 91.55 | 1.20 |
| Fe-Mn-Pb | Pb | 4.63 | 4.56 | 4.83 | 3.70 | 12.18 | 3.29 | 1.06 |
| Al-Fe-Mn | Fe | 258.59 | 239.62 | 367.42 | 39.33 | 1,584.24 | 40.28 | 1.53 |

| | | | | | | | | |
|---|---|---|---|---|---|---|---|---|
| Al-Fe-Mn | Mn | 74.09 | 67.31 | 98.08 | 17.14 | 505.07 | 29.47 | 1.46 |
| Al-Fe-Mn | Al | 58.31 | 54.34 | 83.03 | 30.24 | 368.93 | 12.20 | 1.53 |
| Fe-Mn-Ni | Fe | 4,465.82 | 2,242.40 | 10,928.00 | 166.18 | 16,444.83 | 98.96 | 4.87 |
| Fe-Mn-Ni | Mn | 57.13 | 34.17 | 77.26 | 32.00 | 152.90 | 4.78 | 2.26 |
| Fe-Mn-Ni | Ni | 43.56 | 21.18 | 89.81 | 16.65 | 229.08 | 13.76 | 4.24 |
| Al-Fe-U | Fe | 175.27 | 133.14 | 574.55 | 36.00 | 2,002.14 | 55.62 | 4.32 |
| Al-Fe-U | Al | 68.10 | 55.55 | 119.73 | 35.83 | 481.80 | 13.45 | 2.16 |
| Al-Fe-U | U | 10.38 | 6.52 | 21.74 | 4.57 | 34.79 | 7.61 | 3.33 |

**Table 5. Particle size summary statistics**

| Particle Type | Median | Median Absolute Deviation | Upper CL | Lower CL | Min Value | Max Value |
|---|---|---|---|---|---|---|
| Fe | 87.95 | 14.64 | 88.31 | 87.82 | 67.58 | 531.50 |
| Mn | 61.30 | 12.24 | 61.95 | 61.10 | 46.30 | 169.44 |
| Fe-Mn | 109.88 | 19.24 | 110.75 | 109.57 | 78.97 | 520.96 |
| Al-Fe | 126.12 | 30.07 | 130.24 | 125.47 | 86.02 | 296.39 |
| Al | 67.22 | 4.54 | 67.70 | 66.99 | 60.78 | 176.25 |
| Fe-Mn-Pb | 144.83 | 31.79 | 155.97 | 141.88 | 88.30 | 315.04 |
| Si | 132.98 | 8.07 | 136.23 | 131.79 | 120.59 | 256.80 |
| Fe-U | 87.01 | 13.60 | 92.81 | 86.45 | 73.72 | 201.17 |
| Al-Fe-Mn | 163.20 | 38.20 | 176.66 | 155.23 | 102.37 | 266.43 |
| Fe-Ti | 87.77 | 14.31 | 94.95 | 85.62 | 71.23 | 164.99 |
| Fe-Cu | 121.34 | 42.88 | 136.35 | 106.64 | 77.60 | 248.99 |
| Fe-Ni | 121.45 | 57.75 | 179.29 | 113.04 | 76.24 | 396.73 |
| Fe-Pb | 128.23 | 49.03 | 155.21 | 100.97 | 74.85 | 284.75 |

| | | | | | | |
|---|---|---|---|---|---|---|
| Fe-Mn-Ni | 373.11 | 122.93 | 501.84 | 297.07 | 142.16 | 574.73 |
| Fe-Si | 166.19 | 31.92 | 210.79 | 149.05 | 138.96 | 255.72 |
| Al-Fe-U | 134.64 | 41.43 | 195.75 | 129.27 | 87.86 | 298.56 |
| Mn-Pb | 74.88 | 22.49 | 95.71 | 68.89 | 58.63 | 189.17 |

**Table 6. Particle size summary statistics by number of elements per particle**

| Number of Elements | Median | Median Absolute Deviation | Upper CL | Lower CL | Min Value | Max Value |
|---|---|---|---|---|---|---|
| single | 82.60018 | 16.94153 | 82.88606 | 82.50492 | 46.29926 | 531.4974 |
| two | 111.16809 | 21.93306 | 112.03190 | 110.82059 | 47.69873 | 520.9635 |
| three | 153.21611 | 51.06795 | 160.13473 | 150.21092 | 73.01604 | 574.7344 |

**Table 7. Relative number of particles**

| Site | Particle Category | Site Percentage |
|---|---|---|
| WS | Fe | 45.80 |
| WS | Mn | 11.82 |
| WS | Mn-Fe | 13.18 |
| WS | other_single | 25.09 |
| WS | other_multi | 4.11 |
| CF1 | Fe | 41.79 |
| CF1 | Mn | 23.46 |
| CF1 | Mn-Fe | 15.31 |
| CF1 | other_single | 15.16 |
| CF1 | other_multi | 4.27 |
| CF2 | Fe | 35.80 |
| CF2 | Mn | 27.78 |
| CF2 | Mn-Fe | 21.15 |
| CF2 | other_single | 12.65 |
| CF2 | other_multi | 2.62 |
| CF3 | Fe | 42.31 |
| CF3 | Mn | 20.75 |
| CF3 | Mn-Fe | 19.70 |
| CF3 | other_single | 13.50 |

| | | |
|---|---|---|
| CF3 | other_multi | 3.74 |
| CF4 | Fe | 42.95 |
| CF4 | Mn | 24.12 |
| CF4 | Mn-Fe | 15.99 |
| CF4 | other_single | 12.11 |
| CF4 | other_multi | 4.84 |
| CF5 | Fe | 52.99 |
| CF5 | Mn | 12.60 |
| CF5 | Mn-Fe | 13.31 |
| CF5 | other_single | 16.69 |
| CF5 | other_multi | 4.41 |
| CF6 | Fe | 47.16 |
| CF6 | Mn | 12.69 |
| CF6 | Mn-Fe | 11.41 |
| CF6 | other_single | 24.87 |
| CF6 | other_multi | 3.87 |
| CF7 | Fe | 50.04 |
| CF7 | Mn | 13.05 |
| CF7 | Mn-Fe | 12.36 |
| CF7 | other_single | 19.31 |
| CF7 | other_multi | 5.24 |
| LB | Fe | 68.67 |
| LB | Mn | 2.94 |
| LB | Mn-Fe | 3.00 |
| LB | other_single | 18.20 |
| LB | other_multi | 7.18 |
| CF8 | Fe | 54.03 |
| CF8 | Mn | 9.87 |
| CF8 | Mn-Fe | 12.26 |
| CF8 | other_single | 19.43 |
| CF8 | other_multi | 4.42 |

**Table 8. Generalized additive model fitted values for particle concentration and load.**

| Site | Distance Downstream (km) | Particle Category | Fitted Value (particles $L^{-1}$) | Standard Error | Measurement |
|---|---|---|---|---|---|
| CF1 | 0.00 | Fe | 1.34e+10 | 5.43e+08 | particle concentration |
| CF2 | 5.00 | Fe | 1.35e+10 | 4.93e+08 | particle concentration |
| CF3 | 12.20 | Fe | 1.82e+10 | 5.02e+08 | particle concentration |
| CF4 | 19.30 | Fe | 2.18e+10 | 5.23e+08 | particle concentration |
| CF5 | 30.80 | Fe | 2.14e+10 | 5.45e+08 | particle concentration |
| CF6 | 44.60 | Fe | 2.21e+10 | 5.53e+08 | particle concentration |
| CF7 | 64.20 | Fe | 2.18e+10 | 5.56e+08 | particle concentration |
| CF8 | 77.65 | Fe | 1.64e+10 | 5.61e+08 | particle concentration |
| CF1 | 0.00 | Mn | 9.90e+09 | 6.55e+08 | particle concentration |
| CF2 | 5.00 | Mn | 9.50e+09 | 5.96e+08 | particle concentration |
| CF3 | 12.20 | Mn | 8.92e+09 | 5.21e+08 | particle concentration |
| CF4 | 19.30 | Mn | 8.35e+09 | 4.63e+08 | particle concentration |
| CF5 | 30.80 | Mn | 7.43e+09 | 4.20e+08 | particle concentration |
| CF6 | 44.60 | Mn | 6.32e+09 | 4.67e+08 | particle concentration |
| CF7 | 64.20 | Mn | 4.75e+09 | 6.64e+08 | particle concentration |
| CF8 | 77.65 | Mn | 3.67e+09 | 8.41e+08 | particle concentration |
| CF1 | 0.00 | Fe-Mn | 5.20e+09 | 3.08e+08 | particle concentration |
| CF2 | 5.00 | Fe-Mn | 7.42e+09 | 2.71e+08 | particle concentration |
| CF3 | 12.20 | Fe-Mn | 8.63e+09 | 2.78e+08 | particle concentration |
| CF4 | 19.30 | Fe-Mn | 8.10e+09 | 2.92e+08 | particle concentration |
| CF5 | 30.80 | Fe-Mn | 5.45e+09 | 3.08e+08 | particle concentration |
| CF6 | 44.60 | Fe-Mn | 5.32e+09 | 3.15e+08 | particle concentration |
| CF7 | 64.20 | Fe-Mn | 5.38e+09 | 3.17e+08 | particle concentration |
| CF8 | 77.65 | Fe-Mn | 3.73e+09 | 3.21e+08 | particle concentration |
| CF1 | 0.00 | other_single | 4.56e+09 | 1.20e+09 | particle concentration |
| CF2 | 5.00 | other_single | 5.03e+09 | 9.11e+08 | particle concentration |
| CF3 | 12.20 | other_single | 5.76e+09 | 8.33e+08 | particle concentration |
| CF4 | 19.30 | other_single | 6.56e+09 | 8.95e+08 | particle concentration |
| CF5 | 30.80 | other_single | 8.03e+09 | 9.96e+08 | particle concentration |
| CF6 | 44.60 | other_single | 9.51e+09 | 1.10e+09 | particle concentration |
| CF7 | 64.20 | other_single | 8.50e+09 | 1.10e+09 | particle concentration |
| CF8 | 77.65 | other_single | 6.51e+09 | 1.43e+09 | particle concentration |
| CF1 | 0.00 | other_multi | 1.46e+09 | 2.35e+08 | particle concentration |

| Site | Distance Downstream (km) | Particle Category | Fitted Value (particles $L^{-1}$) | Standard Error | Measurement |
|---|---|---|---|---|---|
| CF2 | 5.00 | other_multi | 1.38e+09 | 1.92e+08 | particle concentration |
| CF3 | 12.20 | other_multi | 2.03e+09 | 2.02e+08 | particle concentration |
| CF4 | 19.30 | other_multi | 2.75e+09 | 2.14e+08 | particle concentration |
| CF5 | 30.80 | other_multi | 2.22e+09 | 2.33e+08 | particle concentration |
| CF6 | 44.60 | other_multi | 2.18e+09 | 2.42e+08 | particle concentration |
| CF7 | 64.20 | other_multi | 2.58e+09 | 2.46e+08 | particle concentration |
| CF8 | 77.65 | other_multi | 1.73e+09 | 2.52e+08 | particle concentration |
| CF1 | 0.00 | Fe | 2.87e+13 | 3.10e+12 | particle load |
| CF2 | 5.00 | Fe | 4.05e+13 | 2.27e+12 | particle load |
| CF3 | 12.20 | Fe | 5.91e+13 | 2.35e+12 | particle load |
| CF4 | 19.30 | Fe | 7.68e+13 | 2.52e+12 | particle load |
| CF5 | 30.80 | Fe | 9.86e+13 | 2.79e+12 | particle load |
| CF6 | 44.60 | Fe | 1.18e+14 | 3.05e+12 | particle load |
| CF7 | 64.20 | Fe | 1.28e+14 | 3.13e+12 | particle load |
| CF8 | 77.65 | Fe | 1.32e+14 | 3.54e+12 | particle load |
| CF1 | 0.00 | Mn | 1.81e+13 | 1.65e+12 | particle load |
| CF2 | 5.00 | Mn | 2.64e+13 | 1.60e+12 | particle load |
| CF3 | 12.20 | Mn | 2.97e+13 | 1.61e+12 | particle load |
| CF4 | 19.30 | Mn | 4.48e+13 | 1.63e+12 | particle load |
| CF5 | 30.80 | Mn | 2.33e+13 | 1.65e+12 | particle load |
| CF6 | 44.60 | Mn | 3.21e+13 | 1.66e+12 | particle load |
| CF7 | 64.20 | Mn | 3.30e+13 | 1.66e+12 | particle load |
| CF8 | 77.65 | Mn | 2.42e+13 | 1.67e+12 | particle load |
| CF1 | 0.00 | Fe-Mn | 1.23e+13 | 1.33e+12 | particle load |
| CF2 | 5.00 | Fe-Mn | 2.00e+13 | 1.10e+12 | particle load |
| CF3 | 12.20 | Fe-Mn | 2.74e+13 | 1.15e+12 | particle load |
| CF4 | 19.30 | Fe-Mn | 2.95e+13 | 1.22e+12 | particle load |
| CF5 | 30.80 | Fe-Mn | 2.51e+13 | 1.32e+12 | particle load |
| CF6 | 44.60 | Fe-Mn | 2.86e+13 | 1.37e+12 | particle load |
| CF7 | 64.20 | Fe-Mn | 3.12e+13 | 1.39e+12 | particle load |
| CF8 | 77.65 | Fe-Mn | 3.01e+13 | 1.43e+12 | particle load |
| CF1 | 0.00 | other_single | 9.34e+12 | 6.32e+12 | particle load |
| CF2 | 5.00 | other_single | 1.34e+13 | 4.86e+12 | particle load |
| CF3 | 12.20 | other_single | 1.95e+13 | 4.34e+12 | particle load |

| Site | Distance Downstream (km) | Particle Category | Fitted Value (particles $L^{-1}$) | Standard Error | Measurement |
|---|---|---|---|---|---|
| CF4 | 19.30 | other_single | 2.59e+13 | 4.62e+12 | particle load |
| CF5 | 30.80 | other_single | 3.71e+13 | 5.17e+12 | particle load |
| CF6 | 44.60 | other_single | 4.89e+13 | 5.69e+12 | particle load |
| CF7 | 64.20 | other_single | 5.21e+13 | 5.71e+12 | particle load |
| CF8 | 77.65 | other_single | 4.99e+13 | 7.59e+12 | particle load |
| CF1 | 0.00 | other_multi | 3.44e+12 | 1.03e+12 | particle load |
| CF2 | 5.00 | other_multi | 4.74e+12 | 8.03e+11 | particle load |
| CF3 | 12.20 | other_multi | 6.62e+12 | 7.09e+11 | particle load |
| CF4 | 19.30 | other_multi | 8.30e+12 | 7.50e+11 | particle load |
| CF5 | 30.80 | other_multi | 1.04e+13 | 8.41e+11 | particle load |
| CF6 | 44.60 | other_multi | 1.22e+13 | 9.22e+11 | particle load |
| CF7 | 64.20 | other_multi | 1.40e+13 | 9.29e+11 | particle load |
| CF8 | 77.65 | other_multi | 1.46e+13 | 1.25e+12 | particle load |

**Table 9. Generalized additive model p-values and r-squared values for particle numerical concentration and load.**

| Particle Category | P-value* | R-Squared* | Measurement |
|---|---|---|---|
| Fe | p<1e-06 | 0.932 | particle concentration |
| Mn | 4.7e-05 | 0.517 | particle concentration |
| Fe-Mn | p<1e-06 | 0.896 | particle concentration |
| other_single | 0.05114 | 0.275 | particle concentration |
| other_multi | 0.003323 | 0.566 | particle concentration |
| Fe | p<1e-06 | 0.973 | particle load |
| Mn | p<1e-06 | 0.881 | particle load |
| Fe-Mn | p<1e-06 | 0.861 | particle load |
| other_single | 0.000332 | 0.550 | particle load |
| other_multi | 2e-06 | 0.722 | particle load |

*These values are based on the significance of the smooth terms of the model.

**Table 10. Generalized additive model fitted values and standard error for element concentration and load.**

| Site | Distance Downstream (km) | Element | Fitted Values | Standard Error | Measurement |
|---|---|---|---|---|---|
| CF1 | 0.00 | Fe | 146.17 | 19.30 | element concentration |
| CF2 | 5.00 | Fe | 165.14 | 14.56 | element concentration |
| CF3 | 12.20 | Fe | 192.24 | 13.39 | element concentration |
| CF4 | 19.30 | Fe | 213.20 | 14.43 | element concentration |
| CF5 | 30.80 | Fe | 230.96 | 16.03 | element concentration |
| CF6 | 44.60 | Fe | 234.43 | 17.72 | element concentration |
| CF7 | 64.20 | Fe | 216.37 | 17.73 | element concentration |
| CF8 | 77.65 | Fe | 182.79 | 22.96 | element concentration |
| CF1 | 0.00 | Mn | 56.09 | 5.75 | element concentration |
| CF2 | 5.00 | Mn | 76.48 | 5.12 | element concentration |
| CF3 | 12.20 | Mn | 83.03 | 5.24 | element concentration |
| CF4 | 19.30 | Mn | 95.89 | 5.49 | element concentration |
| CF5 | 30.80 | Mn | 51.36 | 5.76 | element concentration |
| CF6 | 44.60 | Mn | 54.64 | 5.87 | element concentration |
| CF7 | 64.20 | Mn | 51.45 | 5.91 | element concentration |
| CF8 | 77.65 | Mn | 26.41 | 5.97 | element concentration |
| CF1 | 0.00 | Zn | 0.46 | 0.11 | element concentration |
| CF2 | 5.00 | Zn | 0.56 | 0.08 | element concentration |
| CF3 | 12.20 | Zn | 0.69 | 0.08 | element concentration |
| CF4 | 19.30 | Zn | 0.78 | 0.09 | element concentration |
| CF5 | 30.80 | Zn | 0.78 | 0.10 | element concentration |
| CF6 | 44.60 | Zn | 0.68 | 0.11 | element concentration |
| CF7 | 64.20 | Zn | 0.83 | 0.11 | element concentration |
| CF8 | 77.65 | Zn | 1.18 | 0.13 | element concentration |
| CF1 | 0.00 | Cu | 0.68 | 0.08 | element concentration |
| CF2 | 5.00 | Cu | 0.71 | 0.08 | element concentration |
| CF3 | 12.20 | Cu | 0.75 | 0.07 | element concentration |
| CF4 | 19.30 | Cu | 0.79 | 0.06 | element concentration |
| CF5 | 30.80 | Cu | 0.85 | 0.05 | element concentration |
| CF6 | 44.60 | Cu | 0.93 | 0.06 | element concentration |
| CF7 | 64.20 | Cu | 1.05 | 0.08 | element concentration |
| CF8 | 77.65 | Cu | 1.12 | 0.11 | element concentration |

| Site | Distance Downstream (km) | Element | Fitted Values | Standard Error | Measurement |
|---|---|---|---|---|---|
| CF1 | 0.00 | As | 0.22 | 0.06 | element concentration |
| CF2 | 5.00 | As | 0.26 | 0.05 | element concentration |
| CF3 | 12.20 | As | 0.30 | 0.04 | element concentration |
| CF4 | 19.30 | As | 0.34 | 0.04 | element concentration |
| CF5 | 30.80 | As | 0.36 | 0.05 | element concentration |
| CF6 | 44.60 | As | 0.36 | 0.05 | element concentration |
| CF7 | 64.20 | As | 0.29 | 0.05 | element concentration |
| CF8 | 77.65 | As | 0.18 | 0.07 | element concentration |
| CF1 | 0.00 | Pb | 0.42 | 0.09 | element concentration |
| CF2 | 5.00 | Pb | 0.44 | 0.08 | element concentration |
| CF3 | 12.20 | Pb | 0.46 | 0.07 | element concentration |
| CF4 | 19.30 | Pb | 0.47 | 0.06 | element concentration |
| CF5 | 30.80 | Pb | 0.49 | 0.07 | element concentration |
| CF6 | 44.60 | Pb | 0.49 | 0.07 | element concentration |
| CF7 | 64.20 | Pb | 0.45 | 0.08 | element concentration |
| CF8 | 77.65 | Pb | 0.41 | 0.11 | element concentration |
| CF1 | 0.00 | Fe | 339.39 | 86.60 | element load |
| CF2 | 5.00 | Fe | 462.12 | 66.90 | element load |
| CF3 | 12.20 | Fe | 637.73 | 59.39 | element load |
| CF4 | 19.30 | Fe | 798.22 | 62.97 | element load |
| CF5 | 30.80 | Fe | 1,014.45 | 70.60 | element load |
| CF6 | 44.60 | Fe | 1,199.43 | 77.50 | element load |
| CF7 | 64.20 | Fe | 1,348.58 | 77.91 | element load |
| CF8 | 77.65 | Fe | 1,403.49 | 104.29 | element load |
| CF1 | 0.00 | Mn | 130.46 | 21.32 | element load |
| CF2 | 5.00 | Mn | 205.24 | 18.94 | element load |
| CF3 | 12.20 | Mn | 266.62 | 19.39 | element load |
| CF4 | 19.30 | Mn | 353.05 | 20.34 | element load |
| CF5 | 30.80 | Mn | 231.23 | 21.38 | element load |
| CF6 | 44.60 | Mn | 296.78 | 21.78 | element load |
| CF7 | 64.20 | Mn | 298.28 | 21.93 | element load |
| CF8 | 77.65 | Mn | 212.74 | 22.16 | element load |
| CF1 | 0.00 | Zn | 0.95 | 0.47 | element load |
| CF2 | 5.00 | Zn | 1.49 | 0.35 | element load |

| Site | Distance Downstream (km) | Element | Fitted Values | Standard Error | Measurement |
|---|---|---|---|---|---|
| CF3 | 12.20 | Zn | 2.33 | 0.38 | element load |
| CF4 | 19.30 | Zn | 3.08 | 0.40 | element load |
| CF5 | 30.80 | Zn | 3.67 | 0.44 | element load |
| CF6 | 44.60 | Zn | 3.26 | 0.47 | element load |
| CF7 | 64.20 | Zn | 4.73 | 0.49 | element load |
| CF8 | 77.65 | Zn | 9.78 | 0.52 | element load |
| CF1 | 0.00 | Cu | 1.36 | 0.40 | element load |
| CF2 | 5.00 | Cu | 1.79 | 0.36 | element load |
| CF3 | 12.20 | Cu | 2.41 | 0.31 | element load |
| CF4 | 19.30 | Cu | 3.02 | 0.28 | element load |
| CF5 | 30.80 | Cu | 4.01 | 0.25 | element load |
| CF6 | 44.60 | Cu | 5.19 | 0.28 | element load |
| CF7 | 64.20 | Cu | 6.88 | 0.40 | element load |
| CF8 | 77.65 | Cu | 8.03 | 0.51 | element load |
| CF1 | 0.00 | As | 0.48 | 0.27 | element load |
| CF2 | 5.00 | As | 0.71 | 0.20 | element load |
| CF3 | 12.20 | As | 1.02 | 0.19 | element load |
| CF4 | 19.30 | As | 1.29 | 0.20 | element load |
| CF5 | 30.80 | As | 1.62 | 0.22 | element load |
| CF6 | 44.60 | As | 1.88 | 0.25 | element load |
| CF7 | 64.20 | As | 1.77 | 0.25 | element load |
| CF8 | 77.65 | As | 1.22 | 0.32 | element load |
| CF1 | 0.00 | Pb | 0.95 | 0.39 | element load |
| CF2 | 5.00 | Pb | 1.19 | 0.31 | element load |
| CF3 | 12.20 | Pb | 1.51 | 0.27 | element load |
| CF4 | 19.30 | Pb | 1.82 | 0.27 | element load |
| CF5 | 30.80 | Pb | 2.27 | 0.31 | element load |
| CF6 | 44.60 | Pb | 2.67 | 0.33 | element load |
| CF7 | 64.20 | Pb | 2.83 | 0.35 | element load |
| CF8 | 77.65 | Pb | 2.76 | 0.48 | element load |

**Table 11. Generalized additive model p-values and r-squared values for element concentration and load.**

| Element | P-value | R-squared | Measurement |
|---|---|---|---|
| Fe | 0.027204 | 0.329 | element concentration |
| Mn | 7e-06 | 0.811 | element concentration |
| Zn | 0.007731 | 0.434 | element concentration |
| Cu | 0.009641 | 0.234 | element concentration |
| As | 0.161889 | 0.177 | element concentration |
| Pb | 0.707431 | -0.010 | element concentration |
| Fe | p<1e-06 | 0.776 | element load |
| Mn | 4.8e-05 | 0.757 | element load |
| Zn | p<1e-06 | 0.892 | element load |
| Cu | p<1e-06 | 0.776 | element load |
| As | 0.012356 | 0.383 | element load |
| Pb | 0.011106 | 0.334 | element load |

**Table 12. Limit of detection values for each element**

| Element | LOD |
|---|---|
| Al | 0.4097000 |
| Si | 6.2170000 |
| Ti | 0.2995000 |
| V | 0.0489400 |
| Mn | 0.0214800 |
| Fe | 0.1090000 |
| Ni | 0.0458400 |
| Cu | 0.0426000 |
| Zn | 0.4464000 |
| As | 0.0604200 |
| Cd | 0.0125100 |
| Ba | 0.0180200 |
| La | 0.0005314 |
| Ce | 0.0018820 |
| W | 0.0041840 |
| Au | 0.2260000 |
| Pb | 0.0061770 |
| U | -1,438.0000000 |

**Table 12: Comparison of mass concentrations for Fe vs. Al and Si**

| Site | Mean Fe | Mean Al | Mean Si | Fe:Al Ratio (Fe/Al) | Fe:Si Ratio (Fe/Si) |
|---|---|---|---|---|---|
| CF1 | 155.86 | 3.48 | 8.95 | 44.84 | 17.41 |
| CF2 | 121.26 | 2.57 | 4.35 | 47.11 | 27.89 |
| CF3 | 219.84 | 4.59 | 3.68 | 47.93 | 59.66 |
| CF4 | 228.22 | 5.99 | 3.57 | 38.09 | 63.92 |
| CF5 | 228.38 | 5.38 | 4.88 | 42.45 | 46.82 |
| CF6 | 222.47 | 3.67 | 3.69 | 60.54 | 60.36 |
| CF7 | 236.37 | 5.35 | 6.05 | 44.21 | 39.05 |
| CF8 | 168.90 | 4.38 | 2.64 | 38.54 | 63.98 |
| LB | 157.72 | 5.75 | 3.18 | 27.43 | 49.56 |
| WS | 73.32 | 2.91 | 5.79 | 25.16 | 12.67 |

**Table 13: Comparison of number of particles with Fe vs. Al and Si**

| Site | Number of Particles with Fe | Number of Particles with Al | Number of Particles with Si | Ratio of particle numbers (Fe/Al) | Ratio of particle numbers (Fe/Si) |
|---|---|---|---|---|---|
| CF1 | 430.67 | 37.33 | 6.33 | 11.54 | 68.00 |
| CF2 | 458.67 | 28.00 | 5.33 | 16.38 | 86.00 |
| CF3 | 609.00 | 42.00 | 3.33 | 14.50 | 182.70 |
| CF4 | 696.67 | 60.00 | 4.33 | 11.61 | 160.77 |
| CF5 | 605.33 | 41.67 | 3.67 | 14.53 | 165.09 |
| CF6 | 625.33 | 34.33 | 4.00 | 18.21 | 156.33 |
| CF7 | 629.67 | 54.33 | 4.50 | 11.59 | 139.93 |
| CF8 | 460.00 | 37.00 | 1.67 | 12.43 | 276.00 |
| LB | 450.33 | 62.33 | 2.33 | 7.22 | 193.00 |
| WS | 248.00 | 21.67 | 7.67 | 11.45 | 32.35 |

**Table 14: Load change following mixing of Little Blackfoot and the Clark Fork.**

| Element | Upstream Load (CF7) | Tributary Load (LB) | Downstream Load (CF8) | Percent change in load* |
|---|---|---|---|---|
| Fe | 1,368.27 | 360.45 | 1,363.72 | -26.8 |
| Mn | 298.08 | 16.16 | 212.47 | -47.9 |
| U | 53.78 | 0.53 | 39.76 | -36.6 |
| Ti | 271.79 | 12.97 | 73.43 | -287.8 |
| Ba | 30.63 | 9.08 | 33.79 | -17.5 |
| Ni | 7.20 | 1.59 | 12.10 | 27.4 |
| Al | 30.95 | 13.14 | 35.38 | -24.6 |
| Zn | 4.40 | 1.47 | 9.99 | 41.2 |
| Cu | 6.58 | 0.64 | 8.33 | 13.3 |
| V | 3.58 | 0.78 | 4.77 | 8.63 |
| As | 2.17 | 0.42 | 0.93 | -177.4 |
| Si | 35.04 | 7.27 | 21.32 | -98.5 |
| W | 0.87 | 0.65 | 1.45 | -4.7 |
| Au | 1.57 | 0.93 | 3.43 | 27.1 |
| Pb | 2.91 | 0.17 | 2.45 | -25.7 |

*The percent change in load ($\%\Delta L_x$) for element $x$ was determined as:

$$\%\Delta L_x = \left(\frac{L_{x,CF8}}{L_{x,CF7}+L_{x,LB}} - 1\right) \times 100$$

where $L_{x,CF8}$, $L_{x,CF7}$, and $L_{x,LB}$ are the load for element $x$ at CF8, CF7, and LB, respectively